Fossil biomass preserved as graphitic carbon in a late Paleoproterozoic banded iron formation metamorphosed at more than 550ºC

DOMINIC PAPINEAU[1,2,3], BRADLEY T. DE GREGORIO[4], JAMES SAGAR[1], RICHARD THOROGATE[1], JIANHUA WANG[5], LARRY NITTLER[5], DAVID A. KILCOYNE[6], HUBERTUS MARBACH[7], MARTIN DROST[7], GEOFF THORNTON[1,8]

1 London Centre for Nanotechnology, 17-19 Gordon Street, University College London, London, U.K.

2 Department of Earth Sciences, University College London, London, U.K.

3 Centre for Planetary Sciences, UCL/Birkbeck, London, U.K.

4 Materials Science and Technology Division, U.S. Naval Research Laboratory, Washington DC, U.S.A.

5 Department of Terrestrial Magnetism, Carnegie Institution for Science, Washington, DC, U.S.A.

6 Advanced Light Source, Lawrence Berkeley National Laboratory, Berkeley, CA, U.S.A.

7 Microscopy and Nanolithography Group, Lehrstuhl Für Physikalische Chemie II, Friedrich-Alexander-Universität Erlangen-Nürnberg, Erlangen, Germany.

8 Department of Chemistry, University College London, 20 Gordon Street, London, London U.K.

Revised manuscript submitted for publication in the *Journal of the Geological Society*

Abstract

Metamorphism is thought to destroy microfossils, partly through devolatilization and graphitization of biogenic organic matter. However, the extent to which there is a loss of molecular, elemental, and isotope signatures from biomass during high-temperature metamorphism is not clearly established. We report on graphitic structures inside and coating apatite grains from the ca. 1,850 million years old Michigamme silicate banded iron formation from Michigan, metamorphosed above 550°C. Traces of N, S, O, H, Ca, and Fe are preserved in this graphitic carbon and X-ray spectra show traces of aliphatic groups. Graphitic carbon has an expanded lattice around 3.6Å, forms microscopic radiating rosettes, and has homogeneous $\delta^{13}C$ values around -22‰, identical to bulk analyses. Graphitic carbon inside apatite is associated with nanometre-size ammoniated phyllosilicate. Precursors of these metamorphic minerals and graphitic carbon originated from ferruginous clay-rich sediments with biomass. We conclude that graphite coatings and inclusions in apatite grains indicate fluid remobilization during amphibolite facies metamorphism of precursor biomass. This new evidence fills-in observational gaps of metamorphosed biomass into graphite and supports the existence of biosignatures in the highly metamorphosed iron formation from the Eoarchean Akilia Association, which dates from the beginning of the sedimentary rock record.

Keywords: graphite, metasedimentary, carbon isotopes, biosignature, correlated microscopy.

1. The preservation of biosignatures in graphitic carbon

Understanding the impact of metamorphism on biological organic matter (OM) is a fundamental problem to resolve in order to determine the origin of carbon in the oldest graphite on Earth and in rocks from other ancient planetary surfaces. The metamorphic alteration of OM is known to lead to the loss of heteroatoms and molecular functional groups (Vandenbroucke and Largeau, 2007), as well as to enrichments in heavy carbon and nitrogen isotopes (Desmarais, 2001; Boyd, 2001a). The composition of OM associated with fossils in the rock record can be altered first through diagenesis, when biomass is oxidized by microbes and when sediments are altered by non-equilibrium reactions, dehydration, and eventually by metamorphism. The latter has the greatest effect on the resulting composition and crystallinity because it leads to the graphitization of carbon, in which heteroatoms and light isotopes are lost from biological OM (Bernard and Papineau, 2014). Organic microfossils in Proterozoic rocks metamorphosed at less than 300°C preserve pristine carbon isotope compositions (House et al., 2000; Lepot et al., 2013; Williford et al., 2013; 2015). In fact, carbon isotope compositions are relatively unaffected by metamorphism at conditions less than the greenschist facies (P ca. 3-6 kbar and T ca. 250-450°C), with isotopic fractionations* only about 2 to 4‰ from precursor OM (Desmarais, 2001). Heteroatoms in OM such as H, N, O, and S can also be preserved in OM from microfossils in sedimentary rocks metamorphosed at the greenschist facies (Oehler et al., 2009; 2010) and if they can be quantified, heteroatom concentrations can serve to distinguish types of kerogen (Vandenbroucke et Largeau, 2007). Under high-pressure and temperature below 400°C, organic microfossil structures can still be well-preserved and can contain carboxylic, alcoholic, phenolic, ketonic, and olefinic functional groups (Bernard et al., 2007). Some molecular functional groups may also be preserved through

* Expressed as $\delta^{13}C = \left(\frac{\left(\frac{^{13}C}{^{12}C}\right)_{sample}}{\left(\frac{^{13}C}{^{12}C}\right)_{PDB}} - 1 \right) \times 1000‰$

89 metamorphism up to the amphibolite facies (P ca. 4-9 kbar and T ca. 450-700°C), however
90 alkanes tend to be shorter and less abundant due to thermal cracking (Schwab et al., 2005). It
91 is unknown however if sedimentary rocks metamorphosed at the high-pressure and high-
92 temperature conditions of the amphibolite facies can preserve graphitic carbons with clear
93 biosignatures that indicate a carbon source from biomass. In other words, it is unclear whether
94 combined mineral, molecular, elemental, and isotope signatures can be preserved through such
95 metamorphic regimes and retain diagnostic characteristics of original biomass. This is
96 important, however, because documentation of biological signatures in graphitic carbon from
97 highly metamorphosed rocks serves as a basis to interpret the geobiological record of the oldest
98 sedimentary rocks and to search for biosignatures in extraterrestrial environments.

99 Because animal fossils have never been debated as non-biological in origin and are
100 generally preserved as carbonate-apatite mixtures with OM, clays, and/or pyrite (Olempska
101 and Wacey, 2016), such mineral assemblages in metamorphosed sedimentary rocks can also
102 be indicative of mineralized decayed biomass. Sedimentary rocks from late Palaeoproterozoic
103 age in the Lake Superior area preserve distinct diagenetic structures such as rosettes and
104 granules (LaBerge, 1973; Carrigan and Cameron, 1991; Heaney and Veblen, 1992; Winter and
105 Knauth, 1992; Papineau et al., 2017), microfossils (Barghoorn and Tyler, 1965; Lougheed, 1983;
106 Wacey et al., 2013; Shapiro and Konhauser, 2015), and stromatolites, which demonstrate that
107 microbial ecosystems were widespread in the studied environment. The samples in the current
108 study came from the ca. 1.85 Ga Bijiki member of the Michigamme Formation in the Baraga
109 Group, Michigan, United States, and were metamorphosed at the amphibolite facies. The
110 objective is to provide a comprehensive sub-micron scale documentation of the composition
111 and petrography of graphitic carbon in order to constrain the preservation of biological OM
112 under amphibolite facies metamorphic conditions.

113 The composition of carbon in the amphibolite facies Michigamme banded iron formation
114 (BIF) is also of particular relevance to the controversial origin of carbon in graphite from the

115 3.83 Ga Akilia quartz-pyroxene (Akilia *Qp*) rock, which has been debated as evidence for the
116 earliest life on Earth (Papineau et al., 2010a; 2010b; McKeegan et al., 2007; Nutman and Friend,
117 2006; Mojzsis et al., 1996) and fluid-deposited graphite of possible non-biological origin
118 (Papineau et al., 2010a; Lepland et al., 2002; 2010). The Akilia *Qp* rock is an Fe-silicate BIF
119 metamorphosed at the granulite facies at 3.65 Ga (T > 650^{o}C and P > 5 kBar), retrograded at
120 the amphibolite facies at 2.7 Ga (Manning et al., 2006), and finally around the upper greenschist
121 facies at around 1.5 Ga. Like the Michigamme samples in this study, coarse quartz crystals in
122 the Akilia *Qp* rock are associated with fields of fluid inclusions that commonly contain apatite
123 grains between about 10 and 60 μm, which frequently have graphite coatings (Papineau et al.,
124 2010a). These sizes of apatite crystals are also consistent with analogous apatite occurrences
125 in metapelites from the granulite facies metamorphism in the Lachlan Fold Belt in Australia
126 (Nutman, 2007). The Bijiki graphite is ^{13}C-depleted and contains trace amounts of biologically-
127 important heteroatoms (Papineau et al., 2010b). However, in rocks from such metamorphic
128 grades, graphite can also be associated with calcite, magnetite, multiphase sulphides, and
129 typically enveloped in amphibole, which complicates interpretations of graphite-apatite
130 associations (Papineau et al., 2010a). Thus, the possible biological origin of graphite in the
131 Akilia *Qp* rock remains unclear and debated. Here we make progress on this problem and report
132 new results from the petrologically similar and younger Bijiki BIF that shed some light on the
133 possible biological origin of carbon in graphite from the Akilia *Qp* rock.
134
135 **2. Geology and samples**
136 The Michigamme BIF is just one of several BIF units deposited between 1.85 and 1.83
137 Ga in the Lake Superior region of North America due to hydrothermal and geotectonic activity
138 (Schulz and Cannon, 2007). During the accretion of supercontinent Nuna (Laurentia) in the SW
139 Superior Craton, the Penokean Orogeny resulted in the closure of the Baraga Basin in the
140 Marquette range. These events resulted in the closing of many coeval basins with hydrothermal

141 activity that delivered vast quantities of Fe on the seafloor, now preserved as BIF of the Cuyuna,
142 Mesabi, Iron River, Marquette, Gogebic, and Gunflint ranges. The Penokean Orogen is thought
143 to have ended by 1.84 Ga (Schneider et al., 2002) and to have resulted in the suture of island
144 arcs and the Wisconsin Magmatic Terrain south of the Superior Craton (Van Wyck et al., 1997).
145 Regional volcanism at 1.88 Ga (Rasmussen et al., 2012) was swiftly followed by widespread
146 hydrothermal activity and the deposition of late Paleoproterozoic BIF. Notably, if the Lake
147 Superior BIF are stitched back together, the time-correlative Cuyuna and Mesabi ranges in
148 Minnesota, the Iron River, Gogebic, and Marquette ranges in Michigan, and the Gunflint range
149 of west Ontario would form a continuous, mostly linear belt more than 600 km long of late
150 Paleoproterozoic BIF-pelite-chert successions (Schulz and Cannon, 2007). Collectively, the BIF
151 of the Animikie and Baraga Groups includes various types of mineralogies, including
152 stromatolitic and granular jasper, siderite BIF, grey-red silicate BIF, and grey magnetite cherty
153 BIF and have collectively been metamorphosed at low to high grades, up to the amphibolite and
154 granulite facies in areas of contact metamorphism (French, 1964). Age constraints for the
155 Baraga Group are between 1.874 and 1.833 Ga (Fralick et al., 2002; Rasmussen et al., 2012;
156 Schneider et al., 2002). The location of TVA-294 drill hole is in the area of the Great Lakes
157 tectonic zone in Marquette County in the Upper Peninsula of Michigan, where pre-Penokean
158 rocks have been metamorphosed up to the amphibolite facies during the Penokean Orogen
159 (Holm et al., 2007).

160 Drill core *TVA-294* was drilled by the Ford Motor Company into the Dead River Basin in
161 the Upper Peninsula of Michigan and the studied samples come from a section of this core
162 located between 190 and 200 m depth (621 to 659 feet) (Fig. 1a). The Michigamme Fe-silicate
163 BIF† contains graphite-rich layers (Fig. 1b) as well as pyroxene, grunerite, and magnetite bands
164 with subordinate quartz, biotite, stilpnomelane, chlorite, carbonate, apatite, graphite, pyrite,

† Because of their varied mineralogy and metamorphic grade, Fe-silicate BIF have also been variably called by other workers 'banded silicate formation', 'silicate facies BIF', 'quartz-pyroxene rock' and 'slaty taconite' in the literature.

and pyrrhotite (Fig. 2; Table 1). Associated sedimentary rocks from this drill core contain garnet and inosilicate minerals that confirm metamorphism at the amphibolite facies. Dolomitic carbonate veins in this rock cross-cut layers and contain apatite grains between 5 to 50 μm in size associated with inclusions and coatings of graphitic carbon (Papineau et al., 2010b). In the same rock, apatite grains are concentrated in layers and, based on trace elements of co-occurring graphite, they have been argued to have sourced biomass (Papineau et al., 2010b).

Here we consider the potential contamination by more recent biological activity and fluids. Because Holocene glacial till is preserved as scattered pockets of soils around the Upper Peninsula of Michigan, soils are thin and sparse, and the underlying bedrocks are Late Palaeoproterozoic metasediments. While samples from outcrops are more susceptible to contamination by modern growth, e.g. from lichens and fungus, the studied samples were all from a drill core of Fe ore for the benefit of prospectors for the Ford Motor Company, well separated from the reach of these modern organisms. While phylogenetic analyses suggest that modern microorganisms can colonize and contaminate drill core material (Gérard et al., 2009), these microorganisms are likely only in trace abundance and the timing of their colonization of drill cores remains unknown. Considering the paucity of other sources of biomass younger than the Late Palaeoproterozoic depositional age, we do not expect that young organic molecules could be contaminants in the drill core specimens that we studied. However, contamination by drilling fluids and by late, but not modern, infiltration of OM remains possible and needs to be evaluated in light of the expected crystallinity of graphitic carbons in metamorphosed rocks.

3. Analytical methods

3.1. Micro-Raman spectroscopy

Raman spectroscopy was performed on a separate polished slab, about 1cm diameter by about 0.5 cm in thickness, using a WITec α300 Confocal Raman imaging system at the University College London. A 532 nm laser was used and focused at 1000X magnification for a single acquisition of 100 integrations of 1 second spectra. An optical fibre of 50 microns in diameter was used to collect a Raman spectrum at a confocal depth of 2 μm below the polished surface of a thin section and inside transparent minerals, which minimizes the chances of spectral acquisition with artificially disordered graphite caused by polishing. The resulting average spectrum was corrected with a background subtraction of a polynomial fit of order 4. Raman D1, D2, and G peaks in the spectra were then modelled with Lorentz-fitted curves. The hyperspectral image was created from filters at 965 cm^{-1} width of 20cm^{-1}) for apatite, 1090 cm^{-1} (width 20cm^{-1}) for carbonate, 1575cm^{-1} (width 60cm^{-1}) for graphite, and 1347cm-1 (width 20cm^{-1}) for PCG.

3.2. Focused Ion Beam nanofabrication

Focused ion beam (FIB) milling and lift-out were performed using a FEI Nova 600 dual beam FIB-SEM at the U.S. Naval Research Laboratory. For FIB nanofabrication, a rock slab was shaped into a disk and was polished with 250 nm Al_2O_3 and DI water, rinsed with DI water, rinsed with isopropyl alcohol, dried with a dry N_2 blower, and covered with ca. 10Å Au coat. The polished rock slab, which was never in contact with epoxy, was inserted into the FIB-SEM, and a Pt shield was then deposited on the surface of the target prior to milling. A focused 30 keV Ga^+ primary beam was then used to mill away material from both sides of the deposited Pt shield to expose the lamella. Following lift-out and welding onto an Omniprobe TEM half-grid made of Cu, the lamella was thinned down to approximately 100 nm with progressively smaller beam currents (Wirth, 2009) (down to 20 pA at 30 keV).

3.3. Scanning Electron Microscopy with Energy Dispersive Spectroscopy (SEM-EDS) and Electron Probe Micro-Analysis with Wavelength Dispersive Spectroscopy (EPMA-WDS)

These analyses were performed at the Department of Earth Sciences at University College London using a JEOL JSM-6480L SEM and at the Carnegie Institution of Washington with the JEOL 8900 Superprobe, respectively. In the SEM, the electron beam was set at 0.5 nA and 15 keV, whereas in the EPMA the beam was 5 nA at 30 keV, for spot sizes around 1 μm. The polished rock slab was C-coated prior to EPMA analysis. Abundances were determined in the EPMA using five WDS spectrometers and standards of Durango apatite, and in-house sulphide, garnet, and other silicates, which yield an error of around 0.1 wt% oxide. Other elemental abundances were measured by SEM-EDS at the University College London on Au-coated samples and were obtained from spectra

subtracted of Au, corrected with a XPP matrix correction routine in the Oxford Instruments Inca© software, and normalized to 100.0%, which yields an error around 5%.

3.4. Transmission Electron Microscopy (TEM)

High and low resolution TEM analysis of the lamella was performed with a 200 keV JEOL JEM 2500SE at the Astromaterials Research and Exploration Science e-beam facility at NASA Johnson Space Center (JSC) and with a 200 keV JEOL JEM 2100 in the Department of Chemistry at University College London. The TEM at JSC uses a field emission electron source, while the TEM at UCL uses a LaB_6 electron source. Detailed mineralogy of the FIB lamella was characterized in both conventional bright-field imaging mode and in scanning (STEM) mode using both bright-field (BF, unscattered electrons) and dark field (DF, scattered electrons) detectors. Elemental maps and selected "spot" compositional analyses were acquired at JSC using a Noran energy dispersive X-ray spectrometer (EDS) in STEM mode and at UCL using a liquid nitrogen cooled EDS detector.

3.5. Synchrotron-based Scanning Transmission X-Ray Microscopy (STXM)

Samples were analysed with the polymer STXM beamline 5.3.2.2 at the Advanced Light Source (ALS), Lawrence Berkeley National Laboratory (Kilcoyne et al., 2003). During analysis, the electron current in the storage ring was held constant in "topoff mode" at 500 mA at energy of 1.9 GeV, providing a nearly constant flux of photons at the STXM end-station. The dispersive and non-dispersive exit slits were set at 25 μm. Focusing of the photon beam is produced by a Fresnel zone plate with a spot size of around 30 nm. STXM data were acquired as spectral image stacks (i.e. a series of X-ray absorption images at sequential energies), from which XANES spectra of regions of interest were extracted. The highest spectral resolution (0.1 eV step between subsequent images) was in the 282-292 eV range, where the near-edge spectral features for electronic transitions from core shell states to anti-bonding σ* and π*-orbitals are located. XANES spectra are presented as the ratio of transmission spectra from the region of interest, I, relative to background transmission spectra, I_0, calculated as $A = -\ln(I/I_0)$. Modelling of the CNO spectrum was performed by fitting the Henke mass absorption coefficient curves for those elements to the entire XANES spectrum (Alléon et al. 2015).

3.6. Secondary Ion Mass Spectrometry and NanoSIMS

Secondary Ion Mass Spectrometry (SIMS) analyses were performed on the Gold-coated polished slab, after FIB, but before EPMA analyses and were to measure the $\delta^{13}C$ value of graphite with a Cameca ims 6F ion probe at the Carnegie Institution of Washington. Analytical conditions include extreme energy filtering conditions

(350 eV offset from -5 keV) and the use of the first field aperture and second energy slit. Each analysis consisted of 15 blocks of 10 cycles with a 3σ data rejection of cycles for an analysis time of 25 minutes, including 3 minutes of pre-sputtering. The primary Cs^+ beam current was continuously monitored and kept at 3.0 ± 0.2 nA, to ensure at least 5 x 10^8 counts for the ^{12}C signal, which yielded an internal error better than 0.05%. Spot size was set at 30 μm. The external error was calculated for a bracketing series of spot analyses on an in-house graphite (*BH*-graphite from Sri Lanka (Farquhar et al., 1999); n = 34) and diamond (standard *N198*; n = 15) (Table 2). Reproducibility was calculated as the square root of the sum of the internal error square plus the external error square, and averages ±2.0 ‰ (2σ).

NanoSIMS analyses were performed on the FIB lamella prior to final thinning by Ne. The TEM half-grid with the FIB lamella was mounted on a clean polished Al stub using colloidal silver paint before insertion in the NanoSIMS holder, following the STXM analyses. Analyses were performed as before (Papineau et al., 2010b), but an electron gun was used for charge compensation due to loss of electrons in addition to extracted negative secondary ions, because the FIB lamella is essentially an uncoated insulator. Although a graphite standard was unavailable during these analyses, atomic ratios of C/N and C/O were calibrated using quantitative atomic ratios estimated from STXM measurements on the same areas in the FIB lamella, using the method described by Alléon (2015), and here tentatively applied to also include O/C estimates. We note that there are a number of possible model curves and chose the one that best showed the overall trend of the selected line spectrum. Unfortunately, the NanoSIMS map for O/C was deemed to unreliably show this atomic ratio in graphite due to signal contamination by the phyllosilicate, apatite, and dolomite surrounding the graphitic carbon, a spatial limitation of the technique, which did not enable quantification of the O/C atomic ratio from the CNO-XANES spectrum.

3.7. Helium-Neon Focused Ion Beam milling and microscopy

Surface analyses of the FIB lamella by He-Ne microscopy were performed using a Zeiss Orion NanoFAB FIB instrument located at the London Centre for Nanotechnology at the University College London. Final thinning of the lamella was performed with a 1.6 to 0.8 pA focused beam of Ne^+ and secondary electron images were acquired using a 0.4 pA focused beam of He^+. The He^+ and Ne^+ ions were accelerated to 25 KeV and 15 KeV respectively. Although the decreased Ne acceleration voltage typically results in a larger probe size it has previously been shown that lower landing energies for ion result in increased fidelity of milling (Tan et al., 2010). Organic contamination of the surface of the FIB lamella was minimized by cleaning the Orion NanoFab sample chamber using an oxygen plasma generated by an Evactron® system.

283 *3.8. Atomic Force Microscopy*

284 Atomic Force Microscopy was then used to measure the surface topography and evaluate the roughness
285 of the lamella using a Dimension 3100 system at the London Centre for Nanotechnology at the University College
286 London with the following analytical configuration parameters: Tapping mode AFM (TM-AFM) was carried out on
287 the Dimension 3100 with a Nanoscope IV controller (Bruker Ltd., UK) equipped with a closed loop scanner. PPP-
288 NCH cantilevers (Nanosensors™) with an average spring constant of 42 N/m and a nominal tip radius of curvature
289 <10nm were used for ambient air TM-AFM. The cantilevers were oscillated near their resonant frequency with a
290 free amplitude at resonance of 2V. The amplitude setpoint was set to 80% of the value of the free amplitude.
291 Typical scan rate was 1 Hz.

292

293 *3.9. Auger Electron Spectroscopy*

294 The local Auger Electron Spectroscopy (AES) measurements were performed at room temperature in a
295 UHV chamber (instrument base pressure < $2 \bullet 10^{-10}$ mbar) equipped with a Leo Gemini electron column (resolution
296 < 3 nm) at the Friedrich-Alexander-Universität Erlangen-Nürnberg, Germany. The electron beam of the SEM was
297 used as ionization source, with a beam energy of 15 keV and a nominal probe current of 3 nA. Spectra were
298 recorded with a hemispherical electron energy analyser (EA125, Omicron Nanotechnology) and Matrix 3.1
299 electronics and software (Omicron Nanotechnology). Data processing was performed with Igor Pro 6.22A
300 (Wavemetrics). The depicted spectra were normalized such that both spectra have the same intensity at E_{Kin} = 950
301 eV (i.e. the background level). The quantitative atomic % values given were estimated based on the relevant peak
302 areas (after linear background subtraction) and the corresponding element-specific sensitivity factors of 1.07,
303 0.38, and 0.35 for C, N, and O respectively as theoretically calculated (Mroczkowski and Lichtman, 1985). We note
304 that some re-deposition of milled material onto the FIB lamellae, even after careful Ne thinning, could be included
305 in the spectra; hence we choose to include these results regardless of their validity, as they suggest new analytical
306 possibilities.

307

308 *3.10. Isotope ratio mass spectrometry (IRMS)*

309 Powder from drillates were obtained using a dental drill bur of SiC and 2 mm in diameter and about 2 mm
310 deep, after discarding the first powder generated, which yields about 1-5 mg of rock powder. Samples accurately
311 weighed to μg precision were decarbonated in Ag boats, pre-muffled at 600°C for two hours, using 60-100
312 microliters of sequanal grade 10% HCl (Pierce ©). The decarbonated powders were then dried in a laminar airflow
313 hood for more than 4 days. The samples were then combusted using a Carlo Erba elemental analyser coupled to a

Delta XL IRMS linked with a Conflo III gas injection system at the Carnegie Institution of Washington. Standards of Peru Mud and acetanilide were used to determine the accuracy and, combined with the precision (around 0.05 ‰), yield an error better than 0.3 ‰ consistent with long-term reproducibility of $\delta^{13}C$ values on these phases.

4. Results

4.1. Petrology of graphite and apatite in an amphibolite facies silicate BIF

In thin section, the amphibolite facies Michigamme silicate BIF contains ferrous silicate bands interlayered with magnetite, quartz, and carbonate-rich layers, which can also be rich in OM (Fig. 2a-c; Fig. S1a-b). Occurrences of ferric-ferrous silicates include manganese-bearing proto-ferro-anthophyllite, grunerite, garnet, biotite, stilpnomelane, and green-brown chlorite (Table 1 and Fig. 2c, S1a-S1c). Graphitic carbon in these rocks occurs as massive layers free of clays or sulphides up to about 1 mm in thickness (Fig. 1b), and also as wavy, curvy, and circular filamentous structures in the silicate matrix (Fig. 2d, S2b-S2c) (Papineau et al., 2010b), as coatings and inclusions in about 78% of apatite grains that form in layers parallel to bedding (Papineau et al., 2010b), and as disseminated filamentous fragments in Mn-Fe-dolomite veins and layers (Fig. 2e-f, S2e-S2f). Magnetite grains are less than one mm in size (Fig. 1) and sometimes contain sulphides as micron-size spheroidal inclusions (Fig. S1c). Collectively, the mineral assemblage is consistent with recrystallization under the amphibolite facies conditions.

Raman spectra of both poorly crystalline graphite and well-ordered graphite associated with apatite from elsewhere in this dolomite vein has G-peaks located at 1575 cm^{-1} and D-peaks located around 1347 cm^{-1} (Fig. 3), typical position for graphite and identical to a previous report (Papineau et al., 2010b). The spectrum of well-ordered graphite was used to calculate a maximum metamorphic crystallization temperature (Beyssac et al., 2002a) of 567±50°C, consistent with amphibolite facies metamorphism, and matches graphite with a slightly expanded lattice structure from similar mineral assemblages, previously published from this

rock (Papineau et al., 2010b). Some Raman spectra display a more intense and broad D1 peak than graphitic carbon, but it is unclear whether this is due to polishing artefact (Pasteris et al., 1989), variable structures of turbostratic carbon (Beyssac et al., 2002b), variably crystallized graphitic carbon (Dodd et al., 2019), or possibly also a younger, remobilized, more disordered kind of organic matter. The Raman spectrum shows that this disordered graphitic carbon, or poorly crystalline graphite - PCG from hereon, has the same peak positions for its D1, D2, G, and 2D peaks as the well-ordered graphite (Fig. 3a-b). High-resolution Raman imaging shows the two are finely mixed (inset in Fig. 3a). The calculated crystallization temperature for the PCG was calculated to be 369°C, which may not be accurately estimated, since the Raman thermometer used is based on young organic matter in metapelites (Beyssac et al., 2002a). The PCG is also similar in its Raman spectrum to graphitic carbons found in similarly-aged greenschist to upper greenschist facies rocks elsewhere in the Michigamme Formation and in the Jhamarkotra Formation (Fig. 3c-d).

An apatite grain with graphitic carbon that intersects dolomite from the embedding matrix was targeted for nanofabrication into a lamella with a FIB-SEM (Fig. 2f, S1d-S1f) and subsequently thinned with a Ne beam (Fig. S1g-S1i). Secondary electron images from He ion microscopy, following *in situ* thinning by Ne, show contrast (Fig. 4c) given by the electrical conductivity of the different phases; graphitic carbon appears light grey, except when surrounded by an electrically insulating phase, such as dolomite or apatite. Bright-field TEM images show sub-micron size spherulites of graphite (Fig. 4d) as well as nanoscopic graphite "books" (Fig. 4e). Both of these types of graphitic carbons occur with phyllosilicate (Fig. 4e, S2c). Concentric graphite books have a euhedral habit and intimately co-occur with PCG with a more irregular and patchy texture (Fig. S2k-l). The full range of measured *d*-spacings reveals expanded graphite lattices between 3.55 and 3.72 Å (Fig. 2f; S2i-j). The C-XANES spectra of graphite show well-resolved 285.3 eV and 291.7 eV peaks, and a depressed region in between without strong peaks (Fig. 5c), consistent with highly-ordered graphitic carbon. The presence

366 of these peaks is also akin to graphitic carbons associated with apatite from greenschist to
367 upper greenschist facies in the Michigamme and Jhamarkotra formations (Fig. 5c-d; Papineau
368 et al., 2016; 2017). Hence, both forms of graphitic carbons found by micro-Raman are
369 represented in the FIB lamella, where they are intimately mixed and have a range of *d*-spacings
370 (Fig. 4f).

371 Graphitic carbon is systematically in direct contact with a clay-size, ferrous, crystalline
372 silicate phase (Fig. 4c) that forms a complex and delicate network in apatite and dolomite (Fig.
373 4g). This Fe-silicate phase has 2.08 Å lattice fringes (Fig. S2h) and a composition similar to a
374 calcium end-member of stilpnomelane (Table 1b, Fig. S2e), a ferric-ferrous phyllosilicate with
375 several crystal orientations showing lattice spacings around 2.1 Å (Gruner, 1937; Blake, 1965).
376 We note however that there is only less than 1 wt% Al in this phase, while stilpnomelane is
377 expected to have around 4.3 wt% Al, and hence this phyllosilicate mineral could also be
378 minnesotaite or greenalite. This phyllosilicate is best seen in the contrast offered by He
379 secondary electrons (Fig. 4c) and in X-ray images near the Ca_{2p}–edge (Fig. 5b). Although
380 dolomite, apatite, and silicate minerals are electrical insulators, we suggest that Fe in the
381 phyllosilicate raises its conductivity at the nanometer scale, which yields higher contrast than
382 apatite or dolomite in the secondary electron image from He-microscopy.

383

384 *4.2. Compositions of graphitic carbon and associated phases*

385 The carbon isotope composition of graphite was measured independently by three
386 techniques, all in good agreement. Bulk powder (about 10g) has $\delta^{13}C$ values (Papineau et al.,
387 2010b) around -24.0‰ similar to three 2mm-diameter drilled spots (about 1 mg) that have
388 $\delta^{13}C$ values between -23.4 and -21.4‰ (Fig. 1a), which shows relatively homogeneous
389 compositions over cm scales. A pair of four 30µm diameter spot analyses *in situ* by SIMS, have
390 $\delta^{13}C$ between -21.3 and -22.9‰ (Fig. 2a-b). This graphite layer analysed by SIMS is thus
391 homogeneous with an average $\delta^{13}C_{gra}$ value (n = 10) of -21.7 ± 0.5‰ (1σ) (Table 2). It thus

shows micron-scale homogeneous isotopic compositions over sub-millimetre layers of graphite. This rock is also known to have a $\delta^{13}C_{carb}$ value of -14.9 ‰ (Papineau et al., 2010b).

X-ray images acquired at energies above the photoabsorption energy for C show strong contrast from the graphitic carbon (Fig. 5a), but variable contrast is present within graphitic carbon as well, as shown by X-ray images acquired near the aromatic carbon ($1s \rightarrow \pi^*$) photoabsorption (~285 eV), especially for graphite completely embedded in apatite (Fig. S4b-c). Since the intensity of this π* peak is strongly dependent on the orientation of graphite lattice sheets (Rosenberg et al. 1986), this variable contrast at ~285 eV indicates multiple oriented sub-domains of graphitic carbon, also referred to as highly aromatic carbon. Carbon-XANES spectra from the lamella show no molecular functional group (spectrum 1 in Fig. 5c), whereas some trace residual groups were detected on bulk acid-insoluble OM from the same sample with resolvable peaks at 287.6 and possibly at 288.5 eV (spectra 2 in Fig. 5c). This observation can hardly be attributed to younger contamination, which would be expected to have higher absorption, and they are rather similar to the contemporary occurrences elsewhere in the Michigamme Formation and in the Jhamarkotra Formation. The weak peak at 287.6 eV could represent trace levels of aliphatic C-C bonds (Cody et al., 1996; De Gregorio et al., 2011; Bernard et al., 2012), whereas the peak at 288.5 eV represents the $1s \rightarrow \pi^*$ transition of carboxyl functional groups (Cody et al., 1996; Boyce et al., 2002; Bernard et al., 2012; Ishii and Hitchcock, 1988) and/or interlayer states in the graphite structure (Brandes et al., 2008; Fischer et al., 1991). These two peaks are not unexpected for graphitic carbon metamorphosed at the amphibolite facies, as they are well-resolved in acid insoluble residues from the phosphatic Michigamme chert and Jhamarkotra stromatolite (Fig. 5c), both metamorphosed at the greenschist to upper greenschist facies. It is possible that the PCG could host most of the trace molecular functional groups detected in acid-insoluble residues (Fig. 5c).

The relatively low intensity of these peaks however is consistent with a trace residual abundance due to metamorphism at the amphibolite facies. All samples analysed by STXM also

418 contain N with a peak centred at 404.0 eV, which could point to trace nitro-bearing groups
419 (Alléon et al., 2016; Cody et al., 2011; Papineau et al., 2016), although the feature is broad
420 enough that it could include contributions from many N-bearing organic functional groups (Fig.
421 5d). Other well-resolved peaks are absent from the Bijiki graphitic carbons N-XANES spectra,
422 as well as from the greenschist to upper greenschist facies graphitic carbons of the Jhamarkotra
423 and Michigamme formations (Fig. 5d; *cf.* Papineau et al., 2016). Peaks at 531.7 and 538.9 eV in
424 the O-XANES spectrum may be consistent with C=O functional groups (Hitchcock and Brion,
425 1980) (Fig. S4g). The low intensity of the O-edge relative to that for the phyllosilicate and
426 apatite (Fig. S4g) is consistent with minor O in graphitic carbon. Molecular functional groups
427 commonly found in graphitic carbons of biological origin from the lower greenschist facies
428 Gunflint Formation (De Gregorio et al., 2009; Alléon et al., 2016) and the greenschist to upper
429 greenschist facies Jhamarkotra and Michigamme formations (Papineau et al., 2016; 2017) are
430 therefore also preserved in the amphibolite facies graphitic carbon of the Bijiki BIF, although
431 at significantly lower levels and sometimes undetectable.

432 NanoSIMS secondary ion images reveal the presence of H, N, O and S within graphitic
433 carbons (Fig. 6a-f). The H and N distributions, as seen in the $^{12}C^{1}H$ and $^{12}C^{14}N$ secondary ion
434 images, match the graphitic carbon distribution shown by the ^{12}C secondary ion image (Fig. 6a-
435 c). However, N appears more enriched in graphitic carbon embedded in dolomite than that in
436 apatite (Fig. 6c). Low levels of N also occur in the phyllosilicate and therefore presumably
437 occurs as ammonium (NH_4^+) (Boyd, 2001a; 2001b; Gruner, 1937). Oxygen was detected in all
438 phases including in apatite, dolomite, and phyllosilicate, although it was not clearly resolved in
439 the graphitic carbon by NanoSIMS due to the relative high flux of secondary $^{16}O^-$ ions from
440 associated phases (Fig. 6d; S3a). While no P was detected in dolomite (Fig. 6e), S was detected
441 in relatively high levels in the dolomite, and in trace level in apatite, phyllosilicate, and graphitic
442 carbons where it is non-uniform and tends to form 'hot spots' (Fig. 6f). Structural and chemical
443 heterogeneities are documented in nanoscopic spatial resolutions for all the microscopy

444 techniques used and clearly shows that well-ordered graphite and PCG occur in the FIB lamella
445 and that they contain H, N, O, and S (Fig. 6 and 7).

446 Correlated microscopy can be achieved using semi-transparent and aligned overlays of
447 different images, which can be useful to visualize correlations between nanoscopic chemical
448 heterogeneities and specific mineral phases. This approach is taken here to show the following
449 observations: 1) well-ordered graphite occurs as spherulites and linear books (Fig. 4d, 4e),
450 whereas the associated PCG exhibits variable to random orientations (Fig. 7a), 2) the PCG is
451 mixed with well-ordered graphite and a phyllosilicate resembling stilpnomelane (Fig. 7b), 3)
452 highly aromatic domains are preferentially associated with PCG (Fig 7c, 7l), 4) the Fe-Mg
453 phyllosilicate contains N (Fig. 7d, 7e, 7k), probably as structural ammonium, and 5) PCG
454 contains preferential enrichments of H (Fig. 7g, 7n), N (Fig. 7h, 7k), and S (Fig. 7m). The picture
455 that emerges from this complex and poly-crystalline mixture of graphitic carbons is one where
456 the PCG contains the most compositional heterogeneities in the form of nanoscopic domains
457 with elemental enrichments and where well-ordered graphite has more homogeneous
458 compositions (Fig. 7o). Similar observations of heterogeneous S in graphitic carbon were
459 previously reported in the Akilia *Qp rock*, in which nanoscopic sulphide inclusions occur
460 (Papineau et al., 2010a), and are consistent with partial sulphidization of microorganisms
461 during diagenesis, and the condensation and crystallization of S during metamorphism. We also
462 note the presence of Mn in the apatite with around 0.2 wt% (Table 1a), in phyllosilicates with
463 0.2 to 0.4 wt% (Table 1b), in amphiboles with 1.8 to 2.7 wt% (Table 1c), and in dolomite with
464 4.5 to 6.5 wt% (Table 1d).

465 By fitting a combined CNO-XANES line spectrum collected along the edge of the FIB
466 lamella to a linear combination of tabulated X-ray mass-absorption coefficients (Alléon et al.,
467 2016; Cody et al., 2008) (Fig. S4e), we obtained atomic N/C and O/C ratios of 0.033 ± 0.019 and
468 0.051 ± 0.021, respectively. This method has been used before for the calibration of NanoSIMS
469 elemental ratios in graphitic carbons (Alléon et al., 2015). An artefact in the intensity of

transmitted X-rays between the C-EXAFS region and the N-edge caused a small shift in the spectrum and yielded a poor error of around ±60% for the estimated N/C of graphitic carbon. The STXM line-scan used for the calibration of NanoSIMS secondary ion ratios also had variable O intensities across the graphite (Fig. S4g), which suggests that more accurate calibrations could be achieved for smaller regions of the sample. Using the same line of pixels as that used for the XANES line-scan, we performed a calibration of the atomic N/C ratio measured by NanoSIMS to obtain a quantitative atomic N/C map from secondary ion images (Fig. 6g), which represents an improvement over previous semi-quantitative secondary ion images (Wacey et al., 2013; 2012; Oelher et al., 2010; 2009). In the lamella, the atomic N/C ratio is usually less than 0.04 (Fig. 6g), although there is a highly localized area with N/C ratio up to 0.4, which occurs on the edge of a nanoscopic apatite grain in the lamella (Fig. 6h, 6i). These compositional ratios are higher than previously published measurements by NanoSIMS up to 0.002 in three other graphite occurrences associated with apatite in this same rock and calibrated using a N-bearing graphite standard (Papineau et al., 2010b). These results show that N/C is heterogeneous over three orders of magnitude at sub-micron scales, although most commonly less than 0.04.

Auger Electron Spectroscopy (AES) measures the chemical composition of the first few atomic layers of the sample, hence atomically-flattened surfaces are ideal for chemical analysis with this method (Fig. 8a). Auger electron spectra were acquired from two areas of the lamella for which TEM, STXM, and NanoSIMS data were also acquired (Fig. 8b-c), but after re-thinning the surfaces by Neon. Simultaneous SEM monitoring during the AES measurement ensured that the beam position did not shift significantly during acquisition (Schirmer et al., 2011). Both AES spectra contain electron peaks of C (~ 270 eV), O (~ 510 eV), Fe (~ 654 eV) and Ca (~ 290 eV), while the area marked in red also exhibits a clearly resolved N peak (~ 380 eV – Fig. 8c). Besides the occurrence of N in both graphitic carbon and phyllosilicate, Fe and Ca were also detected in both phases by AES. The spectrum for the phyllosilicate (blue curve in Fig. 8c) has a carbon

peak area more than twice that for graphitic carbon (i.e. ~ 63 at.% vs ~ 25 at.%, respectively), which is interpreted as contamination of the surface by carbon re-deposition and therefore, this Auger data can only be used qualitatively for interpretations. Nevertheless, there are disordered sub-micron domains of graphite and phyllosilicate rich in Ca and N as detected by AES, which independently confirm some TEM, NanoSIMS and STXM observations (Fig. 5b, 6c, 6g, S2f, S4e), and point to co-crystallization with phyllosilicate.

5. Discussion

5.1. Fluid-deposition of apatite with graphitic carbons from carbonic fluids

Metamorphic recrystallization at the amphibolite facies in the Michigamme BIF yielded graphitic carbon associated with stilpnomelane included in and coating manganiferous apatite grains (Table 1a) remobilized in a Mn-dolomite vein cross-cutting sedimentary layering (Fig. 1b). This petrographic context suggests that apatite was fluid-deposited earlier than dolomite and that it was assimilated along with OM from the sedimentary layers and transported in carbonic fluids. Since bulk carbonate has a $\delta^{13}C$ value of -14.9‰ (Papineau et al., 2010b), much of the carbonate in dolomite can be interpreted to be the mineralized product of organic oxidation, as in other BIF (e.g. Heimann et al., 2010). NanoSIMS data also show that trace sulphate is present in dolomite (Fig. 6f), which suggests that it was present in the diagenetic environment and available for possible microbial or thermochemical sulphate reduction. The presence of Mn in dolomite, ankerite, apatite, stilpnomelane, and grunerite from this rock (Table 1) is consistent with dolomite precipitation during decreased alkalinity in the presence of Ca^{2+}, Mg^{2+}, Mn^{2+}, and Fe^{2+} during the remobilization of the carbonic fluids. This probably took place during peak metamorphism. The graphitic carbon inside the apatite and dolomite shows a slightly distorted structure, with expanded lattice spacings between 3.55-3.72 Å (n = 6), which explains the presence of a small D1-peak in the Raman spectra. Using the Raman spectrum acquired from this well-ordered graphite, the peak metamorphic temperature is estimated to

522 be 567±50°C (Fig. 3a) (Beyssac et al., 2002a), consistent with an indigenous source of OM. The
523 presence of H, O, N, and S heteroatoms in both well-ordered graphite and PCG is seen in
524 NanoSIMS images, although it appears that the PCG hosts more trace heteroatoms, and possibly
525 also carboxyl and aliphatic groups.

526 Based on the observation that the Raman spectra of the Michigamme graphite and PCG
527 have the same D1, D2, G, and 2D peak positions, we suggest that both these graphitic carbons
528 have gone through the same metamorphic history. Comparable occurrences of distinct types
529 of graphitic carbons associated with apatite occur in several other Precambrian BIF, and they
530 are most common in highly metamorphosed rocks where fluid-deposition played an
531 important role (Dodd et al., 2019). It is thus possible that both types of graphitic carbons were
532 fluid-deposited and/or directly graphitized from biomass. Hence the PCG is unlikely to
533 represent younger migrated organic matter. This also unlikely because there are no suitable
534 Phanerozoic source rocks in the Michigan Upper Peninsula, and arguments for syngenetic oil
535 generation and migration in the late Palaeoproterozoic sedimentary rocks of the Michigamme
536 Formation have been based on vitrinite reflectance, heteroatom contents, and carbon isotope
537 ratios of "anthraxolite" pyrobitumen (Mancuso et al., 1989). Hence, we find it more likely that
538 the PCG and well-ordered graphite in the Raman spectra differ most likely by having variable
539 levels of functional groups and heteroatoms, and variable ordering possibly due to
540 metamorphic crystallization. Z , whereas graphite likely represents both fluid-deposited and
541 directly graphitized sedimentary organic matter formed during peak metamorphism.

542 Oxidized products of biomass include carbonate and phosphate, which could have
543 initially precipitated as carbonate-apatite layers between silicate- and magnetite-rich BIF
544 layers. Thermal metamorphism during the Penokean Orogen then caused the remobilization of
545 Mn-dolomite into veins, the fluid-deposition of manganiferous apatite (Table 1a), the
546 crystallization of graphitic carbon containing aliphatic groups, the fluid-deposition of graphite
547 spherulites, and the crystallization of stilpnomelane, grunerite, and anthophyllite from ferric-

548 ferrous and manganiferous clay precursors (Tables 1b, 1c). The presence of Mn in the
549 Michigamme BIF is consistent with a syn-depositional hydrothermal-sedimentary source, the
550 same source as Fe, and akin to other manganiferous Precambrian BIF occurrences (Roy, 2006).
551
552 *5.2. Assessing the possible non-biological origins of graphitic carbon and associated minerals*
553 In the context of the search for evidence of early life in metamorphosed sedimentary
554 rocks, the null hypothesis should be evaluated, which means that all possible known non-
555 biological processes should be considered before a biological conclusion can be established.
556 Microscopic spherulites of graphitic carbon preserved in the Bijiki BIF (Fig. 4d) likely formed
557 in part due to the non-biological fluid-deposition of graphite, from the spontaneous reaction of
558 CO_2 and CH_4 either from non-biological mantle sources, or from decomposed microbial biomass
559 (next section). They have a pseudo-hexagonal habit different from that of millimetric graphite
560 spherulites from the Pogranichnoe carbonatite formed from non-biological carbon
561 (Doroshkevitch et al., 2007) and from alkaline pegmatite in the Kola Peninsula with a
562 hydrothermal origin (Jaszczak et al., 2007). Graphite spherulites in both of these Russian
563 occurrences are formed by radially-aligned graphite needles and tubes, whereas the
564 Michigamme graphite forms distinct concentrically-aligned books. In addition, the non-
565 biological graphite from Pogranichnoe and Kola also co-occurs with apatite, showing that these
566 mineral associations can also be non-biological in origin (Doroshkevitch et al., 2007; Jaszczak
567 et al., 2007). Other mantle-fluid processes can also produce non-biological OM associated with
568 apatite as in the case of the Chassigny dunite from Mars where these associated phases have
569 been reported (Papineau, 2012). Instead, the Bijiki graphitic carbon appears unique to
570 sedimentary lithologies and they are similar to graphite filaments from the Jingangku Fm in the
571 ca. 2.5 Ga Wutai Complex of China (Schiffbauer et al., 2007). However, the association of apatite
572 with graphitic carbon can occur through non-biological processes and hence the null

573 hypothesis cannot be rejected for this mineral association nor the morphology of the
574 Michigamme graphitic carbon.

575 To further test the null hypothesis, possible non-biological sources of complex OM could
576 be remobilized to form mantle carbon with an expected $\delta^{13}C$ value around -5‰, characteristic
577 of the upper mantle (Horita, 2005). Graphite can be spontaneously fluid-deposited during the
578 reduction of CO_2 and the oxidation of CH_4 in aqueous fluids (Rumble, 2014), which can lead to
579 the deposition of non-biological graphitic carbon in basalt and pyroxenite on Mars (Steele et al.,
580 2012). Fisher-Tropsch Type (FTT) synthesis can also lead to the formation of short-chain
581 alkanes through catalysis by Cr and Fe-bearing spinels, although Ni-sulphides tend to favour
582 the production of CH_4 over short alkanes (Foustoukos and Seyfried, 2004). Experiments of FTT
583 synthesis show that organic carbon can be significantly depleted in ^{13}C by up to 36‰
584 (McCollom and Seewald, 2007), although in modern hydrothermal systems FTT carbon is not
585 usually depleted by more than 16‰ (Proskorowski et al, 2008). In addition, FTT experiments
586 with variably complex reactants show that various organic compounds containing C, H, O, N,
587 and S can be synthesized non-biologically under hydrothermal conditions (Rushdi and
588 Simoneit, 2004). Because the hydrothermally-influenced environment of the Michigamme BIF
589 is a plausible site for hydrocarbons generated by FTT reactions, the null hypothesis for the
590 isotopic and elemental composition of the graphitic carbon cannot be entirely rejected.

591 It has also been suggested that Mn, Mg, Ca, and Fe-bearing carbonic fluids reacted to
592 form non-biological graphite associated with apatite grains in metasomatically-altered
593 carbonate rocks from the Eoarchean Isua Supracrustal Belt (Lepland et al., 2002). The
594 decarbonation of siderite occurs at temperatures above 450°C and can produce graphite along
595 with magnetite and CO_2 (French, 1971; McCollom, 2003), which could conceivably have re-
596 precipitated as carbonate. Dolomitic carbonate has been proposed as a biosignature (Nutman
597 et al., 2010), although recent carbonation experiments show that clay minerals such as illite
598 and montmorillonite can stimulate the non-biological precipitation of proto-dolomite under

599 ambient conditions (Liu et al., 2019). Similarly, NH_4^+ in phyllosilicates has also been proposed
600 to be a biosignature (Boyd, 2001b), but it could have been sourced from hydrothermal fluids,
601 possibly from non-biological sources such as N_2 reduction with H_2S (Schoonen and Xu, 2001)
602 or the reduction of NO_3^- or NO_2^- with Fe-Ni metals (Summers and Chang, 1993; Brandes et al.,
603 1998; Smirnov et al., 2008). Hence there are known non-biological processes in hydrothermal
604 and metamorphic systems that can result in the precipitation of dolomite with graphitic carbon
605 as well as ammoniated phyllosilicates and therefore the null hypothesis for these biosignatures
606 cannot be rejected.

607 In summary, there are processes under hydrothermal conditions that may produce
608 purely non-biological OM with ^{13}C-depletion, trace elements of H, N, O, and S, and molecular
609 functionalities, or associations with apatite or ammoniated phyllosilicates. However, these non-
610 biological scenarios can only explain some characteristics of the Michigamme graphite and
611 associated minerals; the key fact remains that all observations combined point to a biological
612 origin. A number of non-biological processes can produce the features reported here, but those
613 mechanisms have to converge to coherently explain all the combined key lines of evidence: (1)
614 the geological context in a BIF unit, known to have contemporary versions with prolific
615 stromatolites and microfossils, (2) the presence of syngenetic graphitic carbon with an
616 expanded crystalline structure consistent with metamorphic history, (3) the observed carbon
617 isotope homogeneity, heteroatom heterogeneity, and trace molecular compositions, and (4) the
618 association of graphitic carbon with NH_4^+-bearing phyllosilicate inside apatite, and with
619 sulphate-bearing ^{13}C-depleted dolomite. Indeed, non-biological processes are unlikely to
620 produce all these observed elemental, isotopic, molecular, structural, and mineralogical
621 features documented here together for the metamorphosed Michigamme BIF. Hence, because
622 life had also been present throughout the late Palaeoproterozoic and since at least the
623 Eoarchean, we conclude that a microbial origin is the simplest and most likely explanation for
624 the observed compositions of graphitic carbons and their associated minerals.

625

626 *5.3. The preservation of metamorphosed biological signatures in graphitic carbon*

627 In the Michigamme Formation, the age of peak metamorphism was around 1.833 Ga
628 with the intrusion of various plutons and 1.830 Ga with regional metamorphism (Schulz and
629 Cannon, 2007). The origin of the carbon in the Michigamme graphitic carbon must therefore be
630 indigenous and syngenetic, as is the case for graphite in the Biwabik Formation in northern
631 Minnesota (French, 1964). The degree of crystallinity of graphitic carbon associated with
632 apatite in the Michigamme silicate BIF was significantly modified by thermal metamorphism as
633 seen in the Raman spectrum with a low G-peak position and a weak D1-peak (Fig. 3a),
634 commonly observed in metamorphosed graphitic carbon (Beyssac et al., 2002a; 2002b).

635 We now consider that the Michigamme graphite represents the metamorphosed
636 remains of microorganism and that the most graphitized micron-size domains (e.g. Fig. 4d, 4e)
637 represent microbial biomass that has been partly fluid-deposited (Rumble, 2014). This would
638 have occurred during thermal metamorphism, possibly from dehydration reactions involving
639 phyllosilicate precipitation, CH_4 cracked from alkanes, and CO_2 from oxidized and
640 decarboxylated kerogen. No fluid inclusions have been observed so far in the specimens. Direct
641 graphitization of biomass is proposed for the graphitic carbon associated with phyllosilicate
642 (Fig. 7a, 7b). The graphitic carbon seen in BF-TEM images typically has nanoscopic inclusions
643 of highly aromatic carbon (as seen from the most opaque domains at 285.3 eV; Fig. 7c, 7j, 7l),
644 and contains heterogeneities of N, S, and H (Fig. 7g, 7h, 7m). We observed no nanoscopic
645 inclusions of sulphide inside the graphite (Fig. S2k-S2o). Hence, these observations are
646 consistent with nanoscopic-size chemical heterogeneities observed in biological carbon from
647 chert metamorphosed at sub-greenschist facies in the Gunflint Fm (Wacey et al., 2013). Organic
648 matter from the Gunflint chert also contains heteroatoms of N, O, P, and S as well as aromatic
649 alcohol, phenol, and carboxylic acid functional groups (Alléon et al., 2016; De Gregorio et al.,
650 2009). Residual heteroatoms are largely preserved at the greenschist facies, where H/C is

651 typically between 0.1 and 0.5 (Watanabe et al., 1997; Hayes et al., 1983). The above
652 observations are also consistent with trace element compositions in metamorphosed graphitic
653 carbons from stromatolitic phosphorite and pelite including black shale in the contemporary
654 Aravalli Group, India, which have Raman spectra with significant D1-peaks (Fig. 7 in Papineau
655 et al., 2009) and C-XANES spectra often with resolved peaks for carboxyl, aliphatic, nitrile, and
656 nitro functional groups (Fig. 11 in Papineau et al., 2016).

657 Hence, all characteristics of graphitic carbon and associated minerals in the
658 Michigamme Formation are independently consistent with a biological source of carbon from
659 the original depositional environment, and they include: 1) Raman peaks for graphitic carbon
660 consistent with the metamorphic history and silicate mineral assemblages (Fig. 3), 2) the
661 common filamentous graphite morphology (Fig. 2d) never observed in igneous rocks, where
662 graphite usually forms geometric crystal habits (Jaszczak, et al., 2007; 2003), 3) the slightly
663 expanded graphite lattice spacings (Fig. 4f) consistent with crystallization of an organic
664 precursor with heteroatoms, 4) the trace levels of molecular functional groups in graphitic
665 carbon, which is consistent with the independently detected presence of H, N, O, and Ca (Fig.
666 5c, 5d, 6a-6f, 8c, S4e), and similar to what was observed in kerogen from the Gunflint Fm (Alléon
667 et al., 2016), 5) the heterogeneous distribution of N and S that are concentrated over areas less
668 than 500 nm in size (Fig. 7k, 7m), similar to heterogeneous N distributions in OM from the
669 Gunflint Fm (Wacey et al., 2013), 6) the ^{13}C-depleted Mn-Fe dolomite (down to -14.9‰) in
670 veins that most likely sourced carbonate from diagenetically-oxidized biomass (Papineau et al.,
671 2010b), similar to other BIF (Heimann et al., 2010), 7) the systematic association of graphitic
672 carbon with C- and N-bearing phyllosilicate (Fig. 7h, 7k), which may contain NH_4^+ of biological
673 origin (Boyd, 2001b) such as in co-eval BIF from Minnesota (Blake, 1965), 8) the co-occurrence
674 with manganiferous dolomite, apatite, stilpnomelane, and grunerite (Tables 1) that indicate
675 deposition from fluids with hydrothermally-sourced metals (Roy, 2006), and 9) fractionated
676 $\delta^{13}C$ values consistent with a metamorphic overprint on the signature of photoautotrophic

biomass (Table 2) (Desmarais, 2001). These indications point to the Michigamme graphitic carbons having a biological origin, likely dominated by oxygenic photosynthesis and having formed oil, kerogen, and pyrobitumen during metamorphism (Mancuso et al., 1989). Fluid-deposition during the retrograde phase of peak metamorphism can explain why there is PCG in this rock, which could have formed from devolatilized biomass and reaction products such as CO_2 and CH_4.

The compositions of the Michigamme graphitic carbon are those expected for microbial biomass metamorphosed at the amphibolite facies and thus include trace levels of biological element heterogeneities and carbon isotope distributions that are homogeneous from centimetre to micrometre scales. Heating experiments of acritarch microfossils composed of OM have shown that residual ketone and aldehyde functional groups can be preserved after several days of exposure to temperatures at 500^{o}C, and also that recognizable biological structures are best preserved under anoxic metamorphic conditions, but also under oxic conditions (Schiffbauer et al., 2012). These details are important because they demonstrate key characteristics of kerogen metamorphosed at low metamorphic grades and lead to the conclusion that some elemental and molecular characteristics of degraded biomass can be preserved at high metamorphic grades (Bernard et al., 2009; 2007; Boyce et al., 2002).

In summary for the Michigamme BIF, the oxidative and thermal degradation of photoautotrophic microbial biomass with silicate-rich ferruginous sediments produced kerogen, apatite, dolomite with sulphate, sulphide, and ferric-ferrous oxides like hydromagnetite and phyllosilicates like greenalite and stilpnomelane. These diagenetic minerals were then crystallized graphite during prograde metamorphism, whereas PCG is interpreted to have formed from thermally cracked products that were solubilized, remobilized, and fluid-deposited during amphibolite facies metamorphism, but after peak metamorphism. These processes would have begun with precursor biomass mixed with silica and ferruginous clays, and are now preserved as a complex mixture of fluid-deposited graphite

703 and PCG from residual biomass, mixed with apatite, Mn-Fe-dolomite with sulphate,
704 phyllosilicate with NH_4^+, and associated with mineral reaction products from diagenesis and
705 metamorphism including magnetite, pyrrhotite, biotite, chlorite, and grunerite. However,
706 examples from other highly metamorphosed Fe-silicate BIF and graphitic schists should also
707 be rigorously tested by studying graphite petrology and geochemistry.
708
709 *5.5. Implications for the Akilia Qp rock*
710 Comparisons with graphite from the granulite facies Akilia *Qp* rock should reveal a more
711 extreme effect of metamorphism above 640°C on OM with similar original characteristics.
712 While graphite from the Akilia *Qp* rock has characteristics consistent with a biological origin,
713 the geochemical pathways of fluid-deposited graphite with apatite are unknown for such high-
714 temperature metamorphism, and thus uncertainties persist for possible contributions from
715 non-biological sources of carbon in the Akilia graphite. The key observations of Akilia graphite
716 are listed in Table 3 (Papineau et al., 2010a; 2010b) and include 1) its common association as
717 coatings on apatite in linear fields of fluid inclusions in coarse quartz, suggesting precipitation
718 from fluids, 2) its slightly expanded graphite lattice spacings, consistent with the presence of
719 heteroatoms, 3) its heterogeneous distribution of N and S consistent with similar observations
720 in younger metamorphosed graphitic carbons, 4) its co-occurrence with ^{13}C-depleted calcite,
721 consistent with some oxidized organic matter, 5) its ^{13}C-depleted composition not inconsistent
722 with isotopic fractionation of biomass metamorphosed at the granulite facies, 6) the presence
723 of curled graphite structures consistent with granulite facies thermal metamorphism, and 7)
724 the absence of molecular functional groups in C-XANES spectra that confirm the graphitic
725 nature of the carbon (Papineau et al., 2010a; 2010b), and consistent with a complete removal
726 of residual functional groups at the granulite facies. The PCG shares spectral and compositional
727 similarity with younger graphitic carbons of biological origin, e.g. from the Aravalli Supergroup
728 (Papineau et al., 2009; 2016), and C-XANES spectra for bulk acid-insoluble organic matter in

729 the Bijiki BIF suggest that it could be the host of trace residual functional groups and perhaps
730 also heteroatoms.

731 Fluid-deposited graphitic carbon can form from microbial biomass, possibly from
732 thermally-cracked alkanes and decarboxylated kerogen, and could be associated with ^{13}C-
733 depleted carbonate, hydrated minerals, as well as fluid inclusions in quartz that contain CH_4
734 and CO_2 (Lepland et al., 2010). Collectively, the new observations demonstrate the preservation
735 of molecular, elemental, and isotopic biosignatures in graphitic carbon metamorphosed at the
736 amphibolite facies, and strengthen the case for the biological origin of carbon in graphite from
737 the Akilia *Qp* rock. While some workers have suggested that the protracted metamorphic
738 history of the *Akilia Qp* rock precludes any biogenic interpretation and makes it 'impossible' to
739 prove a biological origin (Lepland et al., 2011), progress can still be achieved as demonstrated
740 in this work. The new observations of graphitic carbons associated with fluid-deposited apatite
741 from the Michigamme Formation show highly similar compositions (Table 3), consistent with
742 slightly lower metamorphic temperatures than in the Akilia *Qp* rock. A continuum of the key
743 characteristics of graphitic carbon observed in biomass metamorphosed at the amphibolite and
744 granulite facies is thus established for the first time.

745

746 **6. Conclusions**

747 In the amphibolite facies Michigamme Fe-silicate BIF, the diagenetic oxidation of
748 biomass along with metamorphism at temperatures in excess of 550^{o}C produced the
749 precursors to the mineralization of Mn-Fe dolomite, graphitic carbons, apatite, and sulphides
750 as well as various ferric-ferrous phases including magnetite, anthophyllite, grunerite, and
751 phyllosilicates. Apatite associated with graphitic carbon in this silicate BIF was fluid-deposited
752 from remobilized carbonic fluids that also contained highly polyaromatic hydrocarbons from
753 oxidized and decarboxylated kerogen. The preservation of graphitic carbon as micron-size
754 coatings and inclusions in apatite grains is likely the result of co-precipitation of apatite,

carbonate, and graphitic carbon from phosphatic and carbonic fluids under amphibolite facies temperatures. The graphitic carbon contains trace levels of heterogeneous H, N, O, and S as well as trace amounts of aliphatic and possibly carboxyl groups. Carbon isotope ratios of graphite layers are homogeneous with a $\delta^{13}C$ around -22‰ in centimetre to micrometre scales, which shows that carbon isotopes were fractionated during prograde metamorphism. It also co-occurs with fine-grained ammoniated phyllosilicate and is embedded in manganiferous apatite and sulphate-bearing dolomite. Because all the expected elemental, isotopic, molecular, mineralogical, and morphological biosignatures of degraded microorganisms occur in the Bijiki member of the Michigamme BIF, the reported data is most consistent with a biological origin. There are also no known non-biological graphitic carbons with comparable petrographic distribution, mineral associations, and geochemical composition, such that the null hypothesis can be reasonably rejected for our combined observations. However, none of the null hypotheses for each independent line of evidence evaluated on its own can be rejected.

These observations shorten the observation gap of graphitic carbon from biological origin between the amphibolite and granulite facies. In the Eoarchean Akilia *Qp* rock, graphite occurs in several forms such as apatite coatings (Papineau et al., 2010a), as hydrothermal mineral associations with calcite (Papineau et al., 2010a), and as fluid inclusions that also contain CO_2 and CH_4 (Lepland et al., 2010). Graphite coatings on apatite grains from the Akilia *Qp* rock could have formed from recrystallized biomass (Papineau et al., 2010b; McKeegan et al., 2007; Nutman and Friend, 2006; Mojzsis et al., 1996), and our new data further supports this interpretation by filling the observational gap between well-characterized kerogen from greenschist facies metamorphism (Alléon et al., 2016; Papineau et al., 2017; 2016; Wacey et al., 2013; De Gregorio et al., 2009), and more highly metamorphosed graphitic carbons at amphibolite facies (Schiffbauer et al., 2007; Beyssac et al., 2002; French, 1964). Graphitic carbon associated with apatite, dolomite, and ferric-ferrous oxides and silicates can constitute a solid biosignature in metamorphosed sedimentary rocks if 1) the geological context is

permissive both from the metamorphic history and the inferred depositional environment and 2) the mineralogical, elemental, isotopic, and molecular signatures of life are preserved with or in graphitic carbon and their abundances and distributions are consistent with the metamorphic grade and analogous occurrences. This robust evaluation of the geological transformation of biomass through thermal metamorphism further paves the way to search for biosignatures in other ancient environments, including ancient planetary surfaces such as Mars.

Acknowledgements

DP acknowledges financial support from the University College London, Carnegie Institution for Science, NASA Astrobiology Institute (grant # NNA04CC09A), NASA Exobiology and Evolutionary Biology Program (grant # NNX08AO16G), NASA Early Career Fellowship Program (grant # NNX12AG14G), and Carnegie of Canada. We thank M. Humphrey for access to drill cores in Marquette, R. Hazen for providing the BH graphite from Sri Lanka for SIMS analyses, M.L. Fogel for access to the CF-EA-IRMS, and R. Stroud and S. Huo for assistance with FIB nano-fabrication. The EPSRC supported the acquisition of the Zeiss Orion NanoFab microscope used in this work (grant # EP/K024701/1 to P. Warburton). STXM data was acquired at the Advanced Light Source, which is supported by the Director, Office of Science, Office of Basic Energy Sciences of the U.S. Department of Energy (under Contract No. DE-AC02-05CH11231). This manuscript benefited from four constructive reviewers and editorial handling by P. Donoghue, who are all thanked for their criticism that improved this paper.

References

806 Alléon, J., Bernard, S., Le Guillou, C., Marin-Carbonne, J., Pont, S., Beyssac, O., McKeegan, K.D.,
807 and Robert, F. (2016) Molecular preservation of 1.88 Ga Gunflint organic microfossils as a
808 function of temperature and mineralogy. *Nature Comm.* 10.1038/ncomms11977.
809 Alléon, J., Bernard, S., Remusat, L., and Robert, F. (2015) Estimation of nitrogen-to-carbon ratios of
810 organics and carbon materials at the submicrometer scale. *Carbon* 84, 290-298.
811 Barghoorn, E.S., Tyler, S.A. (1965) Microorganisms from the Gunflint chert. Science 147, 563-575.
812 Bernard, S., Benzerara, K., Beyssac, O., Brown, G.E., Grauvogel Stamm, L., and Duringer, P. (2009)
813 Ultrastructural and chemical study of modern and fossil sporoderms by Scanning
814 Transmission X-ray Microscopy (STXM). *Rev. Palaeobot. Palyn.* 156, 248-261.
815 Bernard, S., Benzerara, K., Beyssac, O., Menguy, N., Guyot, F., Brown, G.E., Goffe, B. (2007)
816 Exceptional preservation of fossil plant spores in high-pressure metamorphic rocks. *Earth*
817 *and Planet. Sci. Lett.* 262, 257-272.
818 Bernard, S., Wirth, R., Schreiber, A., Schulz, H.-M., and Horsfield, B. (2012) Formation of
819 nanoporous pyrobitumen residues during maturation of the Barnett Shale (Fort Worth
820 Basin). *Intl. J. Coal Geol.* 103, 3-11.
821 Bernard, S. and Papineau, D. (2014) Graphitic carbons and biosignatures. *Elements* 10, 435-440.
822 Beyssac, O., Goffe, B., Chopin, C., and Rouzaud, J.N. (2002a) Raman spectra of carbonaceous
823 material in metasediments: a new geothermometer. *J. Met. Petrol.* 20, 859-871.
824 Beyssac , O., Rouzaud, J.-N. Goffé, B., Brunet, F., and Chopin, C. (2002b) Graphitization in a high-
825 pressure, low-temperature metamorphic gradient: a Raman microspectroscopy and HRTEM
826 study. *Contrib. Mineral. Petrol.* **143,** 19-31.
827 Blake, R.L. (1965) Iron phyllosilicates of the Cuyuna district in Minnesota. *Am. Min.* 50, 148-169.
828 Bontognali, T.R.R., McKenzie, J.A., Warthmann, R.J., and Vasconcelos, C. (2014) Microbially-
829 influenced formation of Mg-calcite and Ca-dolomite in the presence of exopolymeric
830 substances produced by sulphate-reducnig bacteria. *Terra Nova* 26, 72-77.
831 Boyce, C.K., Cody, G.D., and Feser, M. (2002) Organic chemical differentiation within fossil plant
832 cell walls detected with X-ray spectromicroscopy. *Geology* 176, 1-30.
833 Boyd, S.R. (2001a) Nitrogen in future biosphere studies. *Chem. Geol.* 176, 1-30.
834 Boyd, S.R. (2001b) Ammonium as a biomarker in Precambrian metasediments. *Precamb. Res.* 108,
835 159-173.
836 Brandes, J.A., Cody, G.D., Rumble, D., Haberstroh, P., Wirick, S., and Gelinas, Y. (2008) Carbon
837 K-edge XANES spectromicroscopy of natural graphite. *Carbon* **46,** 1424-1434.
838 Brandes, J.A., Boctor, N.Z., Cody, G.D., Cooper, B.A., Hazen, R.M., Yoder, H.S. (1998) Abiotic
839 nitrogen reduction on the early Earth. *Nature* 395, 365– 367.

840 Carrigan, W.J. and Cameron, E.M. (1991) Petrological and stable isotope studies of carbonate and
841 sulfide minerals from the Gunflint Formation, Ontario: evidence for the origin of early
842 Proterozoic iron-formation. *Precamb. Res.* 52, 347-380.
843 Cody, G.D., Botto, R.E., Ade, H., Wirick, S. (1996) The application of soft X-ray microscopy to the
844 in-situ analysis of sporinite in coal. *Intl. J. Coal Geol.* 32, 69-86.
845 Cody, G.D., Alexander, C.M.O'D. Yabuta, H., Kilcoyne, A.L.D., Araki, T., Ade, Dera, P., Fogel,
846 M.L., Militzer, B., and Mysen, B.O. (2008) Organic thermometry for chondritic parent
847 bodies. *Earth and Planet. Sci. Lett.* 272, 446-455.
848 Cody, G.D., Heying, E., Alexander, C.M.O'D., Nittler, L.R., Kilcoyne, A.L.D., Sandford, S.A., and
849 Stroud, R.M. (2011) Establishing a molecular relationship between chondritic and cometary
850 organic solids. *Proc. Nat. Acad. Sci.* 108, 19171-19176.
851 De Gregorio, B.T., Sharp, T.G., Flynn, G.J., Wirick, S., and Hervig, R.L. (2009) A biogenic origin
852 for Earth's oldest putative microfossils. *Geology* 37, 631-634.
853 De Gregorio, B.T., Sharp, T.G., Rushdi, A.I., and Simoneit, B.R.T. (2011) Bugs or gunk? Nanoscale
854 methods for assessing the biogenicity of ancient microfossils and organic matter, in:
855 Golding, S.D., Glikson, M. (Ed.), Earliest Life on Earth: Habitats, Environments, and
856 Methods of Detection. Springer, Dordrecht, Netherlands, pp. 239-289.
857 Desmarais, D. (2001) Isotopic evolution of the biogeochemical carbon cycle during the Precambrian.
858 *Rev. Min. Geochem.* 43, 555-578.
859 Dodd, M.S., Papineau, D., She, Z., Manikyamba, C., Wan, Y., O'Neil, J., Karhu, J., Rizo, H., Pirajno,
860 F. (*in review in EPSL*) Widespread occurrences of variably crystalline ^{13}C-depleted graphitic
861 carbons in banded iron formations. 39 pp.
862 Doroshkevitch, A.G., Wall, F., and Ripp, G.S. (2007) Magmatic graphite in dolomite carbonatite at
863 Pogranichnoe, North Transbaikalia, Russia. *Contrib. Min. Petrol.* **153,** 339-353.
864 Farquhar, J., Hauri, E., and Wang, J. (1999) New insights into carbon fluid chemistry and graphite
865 precipitation: SIMS analysis granulite facies graphite from Ponmudi, South India. *Earth and*
866 *Planet. Sci. Lett.* **171,** 607-621.
867 Fischer D.A., Wentzcovitch R.M., Carr R.G., Continenza A., Freeman A.J. (1991) Graphitic
868 interlayer states – a carbon-K near edge X-ray-absorption fine-structure study. *Phys Rev B*
869 **44,** 1427–1429.
870 Foustoukos, D.I. and Seyfried Jr., W.E. (2004) Hydrocarbons in hydrothermal vent fluids: the role of
871 chromium-bearing catalysts. *Science* 304, 1002-1005.
872 Fralick, P., Davis, D., Kissin, S.A. (2002) The age of the Gunflint Formation, Ontario, Canada: single
873 zircon U-Pb age determinations from reworked volcanic ash. *Can. J. Earth Sci.* 39, 1085-
874 1091.

875 French, B. (1964) Graphitization of organic material in a progressively metamorphosed Precambrian
876 iron formation. *Science* 146, 917-918.
877 French, B.M. (1971) Stability relations of siderite (FeCO3) in the system Fe-C-O, *Am. J. Sci.* 271,
878 37-78.
879 Gérard, E., Moreira, D., Philippot, P., van Kranendonk, M.J., and López-García, P. (2009) Modern
880 subsurface bacteria in pristine 2.7 Ga-old fossil stromatolite drillcore samples from the
881 Fortescue Group, Western Australia. *PLOS One* 4, e5298.
882 Gruner, J.W. (1937) Composition and structure of stilpnomelane. *Am. Min.* 22, 912-925.
883 Hayes, J.M., Wedeking, W., and Kaplan, I.R. (1983) Precambrian organic geochemistry, preservation
884 of the record. In: Schopf WJ (ed) Earth's earliest biosphere. Princeton University Press,
885 Princeton, pp 291-301.
886 Heaney, P.J. and Veblen, D.R. (1991) An examination of spherulitic dubiomicrofossils in
887 Precambrian banded iron formations using the transmission electron microscope. *Precamb.*
888 *Res.* 49, 355-372.
889 Heimann, A., Johnson, C.M., Beard, B.L., Valley, J.W., Roden, E.E., Spicuzza, M.J., and Beukes,
890 N.J. (2010) Fe, C, and O isotope compsoitions of banded iron formation carbonates
891 demonstyra a major role for dissimilatory iron reduction in 2.5 Ga marine environments.
892 *Earth Planet. Sci. Lett.* 294, 8-18.
893 Hitchcock, A.P. and Biron, C.E. (1980) Inner-shell excitation of formaldehyde, acetaldehyde, and
894 acetone studied by electron impact. *J. Elect. Spectr. Rel. Phen.* 19, 231-250.
895 Holm, D.K., Schneider, D.A., Rose, S., Mancuso, C., McKenzie, M., Foland, K.A., and Hodges, K.V.
896 (2007) Proterozoic metamorphism and cooling in the southern Lake Superior region, North
897 America and its bearing in crustal evolution. *Precamb. Res.* 157, 106-126.
898 Horita, J. (2005) Some perspectives on isotope biosignatures for early life. *Chem. Geol.* 218, 171-
899 186.
900 House, C.H., Schopf, J.W., McKeegan, K.D., Coath, C.D., Harrison, T.M., and Stetter, K.O. (2000)
901 Carbon isotopic composition of individual Precambrian microfossils. *Geology* 28, 707-710.
902 Ishii, I. and Hitchcook, A.P. (1988) The oscillator strengths for C1s and O1s excitation of some
903 saturated and unsaturated organic alcohols, acids and esters. *J. Elect. Spectr. Rel. Phen.* 46,
904 55–84.
905 Jaszczak, J.A., Dimovski, S., and Hackney, S.A. (2007) Micro- and nanoscale graphite cones and
906 tubes from Hackman Valley, Kola Peninsula, Russia. *Can. Min.* 45, 379-389.
907 Jaszczak, J.A., Robinson, G.W., Dimovski, S., and Gogtsi, Y. (2003) Naturally occurring graphite
908 cones. *Carbon* 41, 2085-2092.

909 Kilcoyne, A.L.D., Tyliszczak, T., Steele, W.F., Fakra, S., Hitchcock, A.P., Franck, K., Anderson, E.,
910 Harteneck, B., Rightor, E.G., Mitchell, G.E., Hitchcock, A.P., Yang, L., Warwick, T., and
911 Ade, H. (2003) Interferometer-controlled scanning transmission X-ray microscopes at the
912 Advanced Light Source. *J. Synchr. Rad.* 10, 125-136.
913 Kouketsu, Y., Mizukami, T., Mori, H., Endo, S., Aoya, M., Hara, H., Nakamura, D., and Wallis, S.
914 (2014) A new approach to develop the Raman carbonaceous material geothermometer for
915 low-grade metamorphism using peak width. *Island Arc* 23, 33-50.
916 Leinweber, P., Kruse, J, Walley, F.L., Gillespie, A., Eckhardt, K.-W., Bltyh, R.I.R., Regier, T. (2007)
917 Nitrogen k-edge XANES – an overview of reference compounds used to identify 'unknown'
918 organic nitrogen in environmental samples. *J. Synchr. Rad.* 14, 500-511.
919 Lepland, A., Arrhenius, G., and Cornell, D. (2002) Apatite in Early Archean Isua supracrustal rocks
920 in southern West Greenland: its origin, association with graphite and potential as a
921 biomarker. *Precamb. Res.* 118, 221-241.
922 Lepland, A., van Zuilen, M.A., and Philippot, P. (2010) Fluid-deposited graphite and its geobiological
923 implications in early Archean gneiss from Akilia, Greenland. *Geobiology* 9, 2-9.
924 Lepot, K., Williford, K.H., Ushikubo, T., Sugitani, K., Mimura, K., Spicuzza, M., and Valley, J.W.
925 (2013) Texture-specific and isotopic compositions in 3.4 Gyr old organic matter support
926 selective preservation in cell-like structures. *Geochim. Cosmochim. Acta* 112, 66-86.
927 Liu, D., Xu, Y., Papineau, D., Yu, N., Fan, Q., Qiu, X., Wang H. (2019) Experimental evidence for
928 abiotic formation of low-temperature proto-dolomite facilitated by clay minerals.
929 *Geochimica Cosmochimica Acta* **247,** 83-95.
930 Mancuso, J.J., Kneller, W., and Quick, J.C. (1989) Precambrian vein pyrobitumen: Evidence for
931 petroleum generation and migration 2 Ga ago. *Precamb. Res.* **44,** 137-146.
932 Manning, C.E., Mojzsis, S.J., and Harrison, T.M. (2006) Geology, and and origin of supracrustal
933 rocks at Akilia, West Greenland. *Am. J. Sci.* 306, 1-66.
934 McCollom, T.M. (2003) Formation of meteorite hydrocarbons from thermal decomposition of
935 siderite (FeCO3). *Geochim. Cosmochim. Acta* 67, 311-317.
936 McKeegan, K.D., Kudryavtsev, A.B., and Schopf, J.W. (2007) Raman and ion microscopic imagery
937 of graphitic inclusions in apatite from older than 3830 Ma Akilia Supracrustal rocks, west
938 Greenland. *Geology* 35, 591-594.
939 Mojzsis, S.J., Arrhenius, G., McKeegan, K.D., Harrison, T.M., Nutman, A.P., and Friend, C.R.L.
940 (1996) Evidence for life on Earth before 3,800 million years ago. *Nature* 384, 55-59.
941 Mroczkowski, S. and Lichtman, D. (1985) Calculated Auger yields and sensitivity factors for KLL-
942 NOO transitions with 1-10 kV primary beams. *J. Vac. Sci. Tech.* A3, 1860-1865.

943 Nutman, A.P., (2007) Apatite recrystallisation during prograde metamorphism, Cooma, southeast
944 Australia: implications for using an apatite-graphite association as a biotracer in ancient
945 metasedimentary rocks. *Australian J. Earth Sci.* **54,** 981-990.
946 Nutman, A.P. and Friend, C.R.L. (2006) Petrography and geochemistry of apatites in banded iron
947 formation, Akilia, W. Greenland: Consequence for oldest life evidence. *Precamb. Res.* 147,
948 100-106.
949 Oehler, D.Z., Robert, F., Walter, M. R., Sugitani, K., Meibom, A., Mostefaoui, S., and Gibson, E.K.
950 (2010) Diversity in the Archean biosphere: new insights from NanoSIMS. *Astrobiology* 10,
951 413-424.
952 Oehler, D.Z., Robert, F., Walter, M.R., Sugitani, K., Allwood, A., Meibom, A., Mostefaoui, S., Selo,
953 M., Thomen, A., Gibson, E. (2009) NanoSIMS: insights to biogenecity and syngeneity of
954 Archean carbonaceous structures. *Precamb. Res.* 173, 70-78.
955 Olempska, E. and Wacey, D. (2016) Ambient inclusion trails in Palaeozoic crustaceans
956 (Phosphatocopina and Ostracoda). *Palaeogeogr. Palaeoclim. Palaeoecol.* 441, 949-958.
957 Papineau, D., Purohit, R., Goldberg, T., Daohui, P., Shields, G.A., Bhu, H., Steele, A., and Fogel,
958 M.L. (2009) High primary productivity and nitrogen cycling after the Paleoproterozoic
959 phosphogenic event in the Aravalli Supergroup, India. *Precamb. Res.* 171, 37-56.
960 Papineau, D., DeGregorio, B.T., Cody, G.D., Fries, M.D., Mojzsis, S.J., Steele, A., Stroud, R.M.,
961 Fogel, M.L. (2010a) Ancient graphite in the Eoarchean quartz-pyroxene rock from Akilia in
962 southwest Greenland I: Petrographic and spectroscopic characterization. *Geochim.*
963 *Cosmochim. Acta* 74, 5862-5883.
964 Papineau, D., DeGregorio, B.T., Stroud, R.M., Steele, A., Pecoits, E., Konhauser, K., Wang, J., Fogel,
965 M.L. (2010b) Ancient graphite in the Eoarchean quartz-pyroxene rock from Akilia in
966 southern West Greenland II: Isotopic and chemical compositions and comparison with
967 Paleoproterozoic banded iron formations. *Geochim. Cosmochim. Acta* 74, 5884-5905.
968 Papineau, D., DeGregorio, B.T., Cody, G.D., O'Neil, J., Steele, A., Stroud, R.M., and Fogel, M.L.
969 (2011) Young poorly crystalline graphite in the >3.8 Gyr old Nuvvuagittuq banded iron
970 formation. *Nature Geosci.* 4, 376-379.
971 Papineau, D. (2012) Organic matter associated with apatite in Martian meteorite Chassigny, 43rd
972 *Lunar and Planetary Science Conference*, p. 1549.
973 Papineau, D., DeGregorio, B.T., Fearn, S., Kilcoyne, D., McMahon, G., Purohit, R., and Fogel, M.L.
974 (2016) Nanoscale petrographic and geochemical insights on the origin of the
975 Palaeoproterozoic stromatolitic phosphorites from Aravalli Supergroup, India. *Geobiology*
976 14, 3-32.

977 Papineau, D., She, Z., and Dodd, M.S. (2017) Chemically-oscillating reactions during the diagenetic
978 oxidation of organic matter and in the formation of granules in late Paleoproterozoic chert
979 from Lake Superior, *Chemical Geology* **47,** 33-54.
980 Pasteris J. D. (1989) In situ analysis in geological thin-sections by laser Raman microprobe
981 spectroscopy: a cautionary note. *Appl. Spectrosc.* **43,** 567–570.
982 Proskurowski, G., Lilley, M.D., Seewald, J.S., Fruh-Green, G.L., Olson, E.J., Lupton, J.E., Sylva, S.,
983 and Kelley, D.S. (2008) Abiogenic hydrocarbon production at Lost City hydrothermal field.
984 *Science* 319, 604-607.
985 Rasmussen, B., Fletcher, I.R., Bekker, A., Muhling, J.R., Gregory, C.J., Thorne, A.M. (2012)
986 Deposition of 1,88-billion-year-old iron formations as a consequence of rapid crustal
987 growth. *Nature* 484, 498-501.
988 Rosenberg, R.A., Love, P.J., and Rehn, V. (1986) Polarisation-dependent C(K) near-edge x-ray-
989 absorption fine structure of graphite. *Physical Review B* 33, 4034-4037.
990 Roy, S. (2006) Sedimentary manganese metallogenesis in response to the evolution of the Earth
991 system. *Earth Sci. Rev.* 77, 273-305.
992 Rumble, D. (2014) Hydrothermal graphitic carbon. *Elements* 10, 427-433.
993 Rushdi, A.I. and Simoneit, B.R.T. (2004) Condensation reactions and formation of amides, esters,
994 and nitriles under hydrothermal conditions. *Astrobiology* 4, 211-224.
995 Schiffbauer, J.D., Wallace, A.F., Hunter Jr, J.L., Kowalewski, M., Bodnar, R.J., and Xiao, S. (2012)
996 Thermally-induced structural and chemical alteration of organic-walled microfossils: an
997 experimental approach to understanding fossil preservation in metasediments. *Geobiology*,
998 DOI: 10.1111/j.1472-4669.2012.00332.x.
999 Schiffbauer, J.D., Yin, L., Bodnar, R.J., Kaufman, A.J., Meng, F., Hu., J., Shen, B., Yuan, X., Bao,
1000 H., and Xiao, S. (2007) Ultrastructural and geochemical characterization of Archean-
1001 Paleoproterozoic graphitic particles: implications for recognizing traces of life in highly
1002 metamorphosed rocks. *Astrobiology* 7, 684-704.
1003 Schirmer, M., Walz, M.-M., Vollnhals, F., Lukasczyk, T., Sandmann, A., Chen, C., Steinrück, and
1004 H.P. Marbach, H. (2011) Electron-beam-induced deposition and post-treatment processes to
1005 locally generate clean titanium oxide nanostructures on Si (100). *Nanotechnology* 22,
1006 085301.
1007 Schneider, D.A., Bickford, M.E., Cannon, W.F., Schulz, K.J., and Hamilton, M.A. (2002) Age of
1008 volcanic rocks and syndepositional iron formations, Marquette Range Supergroup:
1009 implications for the tectonic setting of Paleoproterozoic iron formations of the Lake Superior
1010 region. *Can. J. Earth Sci.* 39, 999-1012.

1011 Schoonen, M.A.A., Xu, Y., 2001. Nitrogen reduction under hydrothermal vent conditions:
1012 implications for the prebiotic synthesis of C–H–O–N compounds. *Astrobiology* 1, 133–142.
1013 Schulz, K.J. and Cannon, W.F. (2007) The Penokean orogeny in the Lake Superior region. *Precamb.*
1014 *Res.* 157, 4-25.
1015 Schwab, V., Spangenberg, J.E., and Grimalt, J.O. (2005) Chemical and carbon isotopic evolution of
1016 hydrocarbons during prograde metamorphism from 100ºC to 500ºC: case study in the Liassic
1017 black shale formation of Central Swiss Alps. *Geochim. Cosmochim. Acta* 69, 1825-1840.
1018 Shapiro, R.S. and Konhauser, K.O. (2015) Hematite-coated microfossils: primary ecological
1019 fingerprint or taphonomic oddity of the Paleoproterozoic? *Geobiology* 13, 209-224.
1020 Smirnov, A., Hausner, D., Laffers, R., Strongin, D.R., and Schoonen, M.A.A. (2008) Aviotic
1021 ammonium formation in the presence of Ni-Fe metals and alloys and its implication for the
1022 Hadean nitrogen cycle. *Geochem. Trans.* 9, doi:10.1186/1467-4866-9-5.
1023 Steele, A., McCubbin, F.M., Fries, M., Kater, L., Boctor, N.Z., Fogel, M.L., Conrad, P.G.,
1024 Glamoclija, M., Spencer, M., Morrow, A.L., Hammond, M.R., Zare, R.N., Vicenzi, E.P.,
1025 Siljestrom, S., Bowden, R., Herd, C.D.K., Mysen, B.O., Shirey, S.B., Amundsen, H.E.F.,
1026 Treiman, A.H., Bullock, E.S., and Jull, A.J.T. (2012) A reduced organic carbon component
1027 in Martian basalts. *Science Express*, DOI: 10.1126/science.1220715.
1028 Summers, D.P. and Chang, S. (1993) Prebiotic ammonia from reduction of nitrite by iron (II) on the
1029 early Earth. *Nature* 365, 630– 633.
1030 Tan, S., Livengood, R., Hack, P., Hallstein, R., and Shima, D. (2010) Nanomachining with a focused
1031 neon beam: A preliminary investigation for semiconductor circuit editing as failure analysis.
1032 *J. Vac. Sci. Tech. B* 29, 06F604-601.
1033 Van Wyck, N. and Johnson, C.M. (1997) Common lead, Sm-Nd, and U-Pb constraints on
1034 petrogenesis, crustal architecture and tectonic setting of the Penokean orogeny
1035 (Paleoproterozoic) in Wisconsin. *GSA Bulletin* 109, 799-808.
1036 Vandenbroucke, M. and Largeau, C. (2007) Kerogen origin, evolution and structure. *Org. Geochem.*
1037 38, 719-833.
1038 Vasconcelos, C., Warthmann, R. McKenzie, J.A., Visscher, P.T., Bittermann, A.G., and van Lith, Y.
1039 (2006) Lithifying microbial mats in Lagoa Vermelha, Brazil: Modern Precambrian relics?
1040 *Sed. Geol.* 185, 175-183.
1041 Wacey, D., Menon, S., Green, L., Gerstmann, D., Kong, C., McLoughlin, N., Saunders, M., and
1042 Brasier, M. (2012) Taphonomy of very ancient microfossils from the 3400Ma Strelley Pool
1043 Formation and 1900 Ma Gunflint Formation: New insights using a focused ion beam.
1044 *Precamb. Res.* 220-221, 234-250.

Wacey, D., McLoughlin, N., Kilburn, M.R., Saunders, M., Cliff, J.B., and Kong, C. (2013) Nanoscale analysis of pyritized microfossils reveals differential heterotrophic consumption in the ~1.9 Ga Gunflint chert. *Proc. Nat. Acad. Sci.* 110, 8020-8024.

Watanabe, Y., Naraoka, H., Wronkiewicz, D.J., Condie, K.C., and Ohmoto, H. (1997) Carbon, nitrogen and sulphur geochemistry of Archean and Proterozoic shales from the Kaapvaal Craton, South Africa. *Cosmochim. Geochim. Acta* 61, 3441-3459.

Williford, K.H., Ushikubo, T., Schopf, J.W., Lepot, K., Kitajima, K., and Valley, J.W. (2013) Preservation and detection of microstructural and taxonomic correlations in the carbon isotopic compositions of individual Precambrian microfossils. *Geochim. Cosmochim. Acta* 104, 165-182.

Williford, K.H., Ushikubo, T., Lepot, K., Kitajima, K., Hallmann, C., Spicuzza, M.J., Kozdon, R., Eigenbrode, J.L., Summons, R.E., and Valley, J.W. (2015) Carbon and sulfur isotopic signatures of ancient life and environment at the microbial scale: Neoarchean shales and carbonates. *Geobiology* DOI: 10.1111/gbi.12163.

Winter, B.L. and Knauth, L.P. (1992) Stable isotope geochemistry of cherts and carbonates from the 2.0 Ga Gunflint iron formation: implications for the depositional setting, and the effects of diagenesis and metamorphism. *Precamb. Res.* 59, 283-313.

Wirth, R. (2009) Focused Ion Beam (FIB) combined with SEM and TEM: Advanced analytical tools for studies of chemical composition, microstructure and crystal structure in geomaterials on a nanometer scale. *Chem. Geol.* 261, 217-229.

Author contributions

D.P. designed and led the research and participated in all analyses; D.P., B.T.D., and D.A.K. performed STXM analyses; D.P. and B.T.D. performed FIB nanofabrication and STEM-EDS analyses; J.S. performed He-Ne FIB nano-fabrication and microscopy; D.P. performed sample preparation and CF-EA-IRMS analyses; R.T. performed the AFM analyses; H.M. and M.D. performed the AES and analysed the data along with G.T.; D.P. and J.W. performed SIMS analyses, L.R.N. contributed to the analysis of NanoSIMS data collected by D.P. and J.W.; D.P. wrote the paper with significant input from all co-authors who also variably contributed to the analysis of the data.

Figures – see attached

Tables

- **Table 1:** X-ray-based compositional analyses of Michigamme minerals using different electron beam instruments.
- **Table 2:** In situ carbon isotope analyses by SIMS on graphite band from TVA294-659.6 and standards.
- **Table 3:** Comparative table of mineralogical and geochemical data between the Michigamme BIF and the Akilia *Qp* rock.

Supplementary information

- **Figure S1: Additional petrographic context.**
- **Figure S2: Compositional and structural analysis of graphite and associated minerals.**
- **Figure S3: Additional contextual images and analysis details of the analysed area used to calibrate NanoSIMS $^{12}C^{14}N^{-}/^{12}C^{-}$ map with STXM.**
- **Figure S4: Additional STXM data of the analyzed target.**
- **Figure S5: Selected line profiles measured by AFM**.

Table 1

Table 1: Elemental compositions of apatites, carbonates, and silicates obtained from EDS and WDS analyses.

a) Apatites analyzed by WDS in the EPMA

Targets	TVA294-659.6	TVA294-659.6	TVA294-659.6	TVA294-659.6
element Wt.(%) / spot	3	12	14	4
CaO	55.1	54.5	55.0	55.1
P_2O_5	41.2	41.5	40.6	40.9
F	3.2	3.2	3.3	3.2
Cl	0.0	0.0	0.0	0.0
FeO	0.5	0.6	1.0	0.4
MnO	0.2	0.3	0.2	0.2
Na_2O	0.0	0.0	0.0	0.0
MgO	0.0	0.0	0.0	0.0
SiO_2	0.0	0.0	0.0	0.0
Ce_2O_3	0.1	0.1	0.0	0.1
Y_2O_3	0.0	0.0	0.0	0.0
Total	99.1	98.8	98.8	98.7
	fluorapatite	fluorapatite	fluorapatite	fluorapatite

b) Fe-silicates analyzed by EDS in the TEM (on FIB lamellae)

Targets	TVA294-656.9	TVA294-656.9
element Wt.(%) / spot	01b	01a
O K	48.6	49.9
Mg K	0.4	0.4
Al K	0.8	0.5
Si K	36.9	39.6
Ca K	0.7	0.8
Mn K	0.4	0.2
Fe K	12.2	8.6
Total	100.0	100.0
	Ca-Mn-stilpnomelane	Ca-Mn-stilpnomelane

c) Ferric-ferrous silicates analysed by EDS in the SEM

Targets	TVA294-622.1	TVA294-622.1	TVA294-622.1	TVA294-622.1	TVA294-622.1	TVA294-622.1	TVA294-622.1
element Wt.(%) / spot	1	2	5	8	7	4	6
C K			14.3				13.0
O K	36.2	36.1	36.3	37.1	39.9	39.2	37.8
Mg K	5.9	5.2	4.1	5.6	5.5	5.1	4.0
Al K					11.2	8.9	8.2
Si K	26.9	26.2	19.5	25.6	12.6	13.9	10.1
K K						1.4	
Mn K	2.3	1.8	1.9	2.7			
Fe K	28.8	30.7	24.0	29.1	30.8	31.5	26.9
Totals	100.0	100.0	100.0	100.0	100.0	100.0	100.0
	proto-Mn,Fe-anthophylite	Mn,Fe-anthophylite	Mn,Fe-anthophyllite + graphite	grunerite	chlorite	chlorite	graphite with chlorite

d) Sulphides and oxides with graphitic carbon analysed by EDS in the SEM

Targets	TVA294-622.1	TVA294-622.1	TVA294-622.1	TVA294-622.1
element Wt.(%) / spot	1	3	9	2
C K		22.4		8.8
O K			11.5	22.9
S K	34.7	26.7	22.3	
Fe K	65.3	50.9	66.2	68.3
Totals	100.0	100.0	100.0	100.0
	pyrrhotite	pyrrhotite + graphite	oxidised pyrite	magnetite + graphite

e) carbonates analysed by EDS in the SEM

Targets	TVA294-656.9	TVA294-656.9	TVA294-622.1	TVA294-622.1	TVA294-622.1	TVA294-622.1
element Wt.(%) / spot	1	2	4	5	6	3
C K	15.5	13.6	13.6	13.6	11.7	63.2
O K	43.0	34.4	43.2	43.2	45.1	20.9
Mg K	9.8	9.8	6.1	6.1	6.7	2.2
Cl K					1.4	
Ca K	26.0	24.8	21.4	21.4	20.7	7.9
Si K	1.1	1.1				0.6
Mn K	4.5	4.9	6.5	6.5	5.4	2.5
Fe K		11.0	9.2	9.2	9.2	2.8
Totals	99.9	99.6	100.0	100.0	100.0	100.0
	Mn-dolomite	Mn-Fe-dolomite	Mn-Fe-dolomite	Mn-Fe-dolomite	Mn-Fe-dolomite	graphite in dolomite

Table 2: In situ carbon isotope analyses on graphite band from TVA294-659.6 and stan

Analysis #	Analysis spot name	$^{13}C/^{12}C$ (uncorr.)	err.	^{12}C count rate (c/s)	^{12}C counts
1	N198a@2.ais	1.04659E-02	4.12E-06	8.67E+05	1.30E+08
2	N198a@3.ais	1.04666E-02	4.53E-06	8.72E+05	1.31E+08
3	N198a@4.ais	1.04786E-02	4.18E-06	8.68E+05	1.30E+08
4	N198a@5.ais	1.04638E-02	4.08E-06	8.69E+05	1.30E+08
5	N198a@6.ais	1.04796E-02	3.87E-06	8.64E+05	1.30E+08
6	N198a@7.ais	1.04731E-02	4.14E-06	8.22E+05	1.23E+08
7	N198a@8.ais	1.04715E-02	3.39E-06	8.49E+05	1.27E+08
8	N198a@9.ais	1.04735E-02	4.04E-06	8.56E+05	1.28E+08
9	N198a@10.ais	1.04856E-02	3.97E-06	8.62E+05	1.29E+08
10	N198a@11.ais	1.04895E-02	4.34E-06	8.65E+05	1.30E+08
11	N198a@12.ais	1.04829E-02	4.40E-06	8.57E+05	1.29E+08
12	N198a@13.ais	1.04928E-02	4.27E-06	8.56E+05	1.28E+08
13	N198a@14.ais	1.04770E-02	4.50E-06	8.43E+05	1.26E+08
14	N198a@15.ais	1.04857E-02	4.09E-06	8.44E+05	1.27E+08
15	N198a@16.ais	1.04869E-02	4.44E-06	8.50E+05	1.27E+08
16	BH_graphite@1.ais	1.04838E-02	4.73E-06	7.24E+05	1.09E+08
17	BH_graphite@2.ais	1.04950E-02	4.54E-06	7.05E+05	1.06E+08
18	BH_graphite@3.ais	1.04853E-02	4.11E-06	7.20E+05	1.08E+08
21	BH_graphite@6.ais	1.04610E-02	4.90E-06	6.03E+05	9.04E+07
22	BH_graphite@7.ais	1.04700E-02	5.30E-06	6.16E+05	9.23E+07
23	BH_graphite@8.ais	1.04810E-02	4.66E-06	6.06E+05	9.09E+07
24	BH_graphite@9.ais	1.04799E-02	4.79E-06	6.23E+05	9.35E+07
25	BH_graphite@10.ais	1.04781E-02	4.72E-06	6.21E+05	9.32E+07
26	BH_graphite@11.ais	1.04712E-02	4.40E-06	6.21E+05	9.31E+07
34	BH_graphite@12.ais	1.04775E-02	4.88E-06	5.89E+05	8.84E+07
35	BH_graphite@13.ais	1.04899E-02	4.83E-06	5.74E+05	8.60E+07
36	BH_graphite@14.ais	1.04869E-02	4.91E-06	5.61E+05	8.41E+07
37	BH_graphite@15.ais	1.04739E-02	5.13E-06	5.16E+05	7.73E+07
38	BH_graphite@16.ais	1.04632E-02	5.79E-06	5.39E+05	8.09E+07
39	BH_graphite@17.ais	1.04860E-02	5.27E-06	5.12E+05	7.68E+07
46	BH_graphite@18.ais	1.04743E-02	5.12E-06	5.24E+05	7.86E+07
47	BH_graphite@19.ais	1.04901E-02	5.30E-06	5.04E+05	7.56E+07
48	BH_graphite@20.ais	1.04813E-02	5.32E-06	5.09E+05	7.63E+07
54	BH_graphite2@1.ais	1.04712E-02	4.83E-06	6.97E+05	1.05E+08
55	BH_graphite2@2.ais	1.04774E-02	4.45E-06	7.17E+05	1.08E+08
56	BH_graphite2@3.ais	1.04744E-02	4.59E-06	7.31E+05	1.10E+08
67	BH_graphite2@4.ais	1.04792E-02	4.71E-06	7.28E+05	1.09E+08
68	BH_graphite2@5.ais	1.04674E-02	4.59E-06	7.35E+05	1.10E+08
69	BH_graphite2@6.ais	1.04747E-02	4.38E-06	7.43E+05	1.11E+08
70	BH_graphite2@7.ais	1.04716E-02	4.10E-06	7.46E+05	1.12E+08
71	BH_graphite2@8.ais	1.04647E-02	4.49E-06	7.33E+05	1.10E+08
72	BH_graphite2@9.ais	1.04865E-02	4.72E-06	7.12E+05	1.07E+08
73	BH_graphite2@10.ais	1.04899E-02	4.55E-06	7.10E+05	1.07E+08
74	BH_graphite2@11.ais	1.04971E-02	4.76E-06	6.75E+05	1.01E+08
79	BH_graphite2@13.ais	1.04540E-02	4.95E-06	5.81E+05	8.71E+07
80	BH_graphite2@14.ais	1.04561E-02	5.28E-06	5.81E+05	8.72E+07

88	BH_graphite2@17.ais	1.04880E-02	5.05E-06	5.36E+05	8.04E+07
106	BH_graphite2@20.ais	1.04763E-02	4.67E-06	5.49E+05	8.23E+07
107	BH_graphite2@21.ais	1.04660E-02	4.66E-06	5.65E+05	8.48E+07
108	BH_graphite2@22.ais	1.04711E-02	5.01E-06	5.63E+05	8.44E+07
57	TVA294-6596@1.ais	1.03354E-02	5.36E-06	5.73E+05	8.60E+07
58	TVA294-6596@2.ais	1.03385E-02	5.03E-06	5.89E+05	8.83E+07
59	TVA294-6596@3.ais	1.03297E-02	4.93E-06	5.78E+05	8.68E+07
60	TVA294-6596@4.ais	1.03323E-02	5.47E-06	5.71E+05	8.57E+07
61	TVA294-6596@5.ais	1.03359E-02	4.95E-06	5.98E+05	8.97E+07
62	TVA294-6596@6.ais	1.03383E-02	4.56E-06	5.92E+05	8.88E+07
63	TVA294-6596@7.ais	1.03362E-02	5.73E-06	5.56E+05	8.34E+07
64	TVA294-6596@8.ais	1.03347E-02	6.08E-06	5.29E+05	7.94E+07
65	TVA294-6596@9.ais	1.03220E-02	5.34E-06	5.31E+05	7.96E+07
66	TVA294-6596@10.ais	1.03383E-02	5.38E-06	4.94E+05	7.41E+07

* The two in-house standards used were diamond N198 ($\delta^{13}C$ = -6.0‰, IMF correction fa

dards*.

I primary (nA)	$^{13}C/^{12}C$ (IMF corr.	$\delta^{13}C$ (‰)	int err (1 σ)	ext err (2 σ)
3.27	1.11208E-02	-9.2	0.4	2.0
3.25	1.11215E-02	-9.2	0.4	2.0
3.21	1.11343E-02	-8.0	0.4	2.0
3.18	1.11186E-02	-9.4	0.4	2.0
3.16	1.11354E-02	-8.0	0.4	2.0
3.08	1.11284E-02	-8.6	0.4	2.0
3.12	1.11267E-02	-8.7	0.3	2.0
3.14	1.11289E-02	-8.5	0.4	2.0
3.09	1.11417E-02	-7.4	0.4	2.0
3.12	1.11459E-02	-7.0	0.4	2.0
3.11	1.11389E-02	-7.6	0.4	2.0
3.06	1.11494E-02	-6.7	0.4	2.0
3.08	1.11326E-02	-8.2	0.4	2.0
3.09	1.11418E-02	-7.4	0.4	2.0
3.05	1.11431E-02	-7.3	0.4	2.0
3.04	1.11398E-02	-7.6	0.5	2.1
3.02	1.11517E-02	-6.5	0.4	2.0
2.99	1.11414E-02	-7.4	0.4	2.0
3.11	1.11156E-02	-9.7	0.5	2.1
3.07	1.11252E-02	-8.9	0.5	2.1
3.03	1.11368E-02	-7.8	0.4	2.1
2.84	1.11357E-02	-7.9	0.5	2.1
2.76	1.11338E-02	-8.1	0.5	2.1
2.92	1.11264E-02	-8.7	0.4	2.0
3.30	1.11331E-02	-8.1	0.5	2.1
3.28	1.11463E-02	-7.0	0.5	2.1
3.27	1.11431E-02	-7.3	0.5	2.1
3.04	1.11293E-02	-8.5	0.5	2.1
3.04	1.11179E-02	-9.5	0.6	2.2
3.03	1.11422E-02	-7.3	0.5	2.1
2.96	1.11297E-02	-8.5	0.5	2.1
2.94	1.11465E-02	-7.0	0.5	2.1
2.90	1.11372E-02	-7.8	0.5	2.1
3.49	1.11264E-02	-8.7	0.5	2.1
3.47	1.11330E-02	-8.2	0.4	2.0
3.44	1.11298E-02	-8.4	0.4	2.0
3.30	1.11349E-02	-8.0	0.4	2.1
3.27	1.11224E-02	-9.1	0.4	2.1
3.26	1.11301E-02	-8.4	0.4	2.0
3.23	1.11269E-02	-8.7	0.4	2.0
3.22	1.11195E-02	-9.4	0.4	2.0
3.20	1.11427E-02	-7.3	0.4	2.1
3.22	1.11463E-02	-7.0	0.4	2.0
3.21	1.11539E-02	-6.3	0.5	2.1
3.07	1.11081E-02	-10.4	0.5	2.1
3.09	1.11104E-02	-10.2	0.5	2.1

3.08	1.11443E-02	-7.2	0.5	2.1
2.83	1.11318E-02	-8.3	0.4	2.1
2.88	1.11209E-02	-9.2	0.4	2.1
2.82	1.11263E-02	-8.8	0.5	2.1
3.43	1.09821E-02	-21.6	0.5	2.1
3.39	1.09854E-02	-21.3	0.5	2.1
3.41	1.09761E-02	-22.1	0.5	2.1
3.38	1.09788E-02	-21.9	0.5	2.1
3.33	1.09827E-02	-21.6	0.5	2.1
3.34	1.09852E-02	-21.3	0.4	2.1
3.31	1.09830E-02	-21.5	0.6	2.2
3.34	1.09814E-02	-21.7	0.6	2.2
3.33	1.09679E-02	-22.9	0.5	2.1
3.32	1.09852E-02	-21.3	0.5	2.1

actor is -60.8‰) and BH-graphite ($\delta^{13}C$ = -8.2‰, IMF correction factor is -58.9‰)

Table 3: Comparative table of mineralogical and geochemical data between the Michigamme BIF and the Akilia Qp rock.

	Amphibolite facies Michigamme silicate BIF	**Granulite facies Akilia Qp rock***
Age	ca. 1.85 Ga	>3.83 Ga
Metamorphic temperature	T = 567±50°C	T > 635°C
Mineralogy	Grunerite, magnetite, quartz, pyroxene, dolomite, stilpnomelane, chlorite, biotite, graphite, apatite, pyrrhotite, pyrite	Quartz, pyroxene (hedenbergite-ferrosilite), magnetite, grunerite-hornblende, calcite, apatite, graphite, pyrrhotite, chalcopyrite, pentlandite,
Specific mineral associations with graphitic carbon	Apatite, dolomite, magnetite, stilpnomelane, grunerite, chlorite, pyrrhotite	Apatite, calcite, magnetite, hornblende, chalcopyrite, pyrrhotite
$\delta^{13}C_{carb}$	-14.9‰*	-3.3. to -5.5‰
$\delta^{13}C_{gra}$	-21.3 to -24.0‰	-4.1 to -49.0‰
Crystallinity of graphitic carbon	D-bands between 1346 and 1353 cm^{-1} (FWHM between 41 and 51 cm^{-1} and between 82 and 85 cm^{-1}) and G-bands between 1574 to 1581 cm^{-1} (FWHM between 41 and 77 cm^{-1}) *	D-bands between 1344 and 1358 cm^{-1} (FWHM between 22 and 29 cm^{-1}) and G-bands between 1573 to 1581 cm^{-1} (FWHM between 10 and 46 cm^{-1}); presence of curled graphite structures
d-spacing of graphitic carbon	3.55-3.72Å	3.41-3.64Å
Atomic N/C in graphitic carbon	10^{-4} to 10^{-1}	10^{-6} to 10^{-4}
Heteroatoms in graphitic carbon	H, N, O, S, P, Ca, Fe	H, N, O, S, P, Fe
Molecular functional groups	Aliphatic and carboxyl (both minor)	None detected

* Data from Papineau et al. (2010b) and Papineau et al. (2010a)

Figure 1 – Papineau et al. (2019)

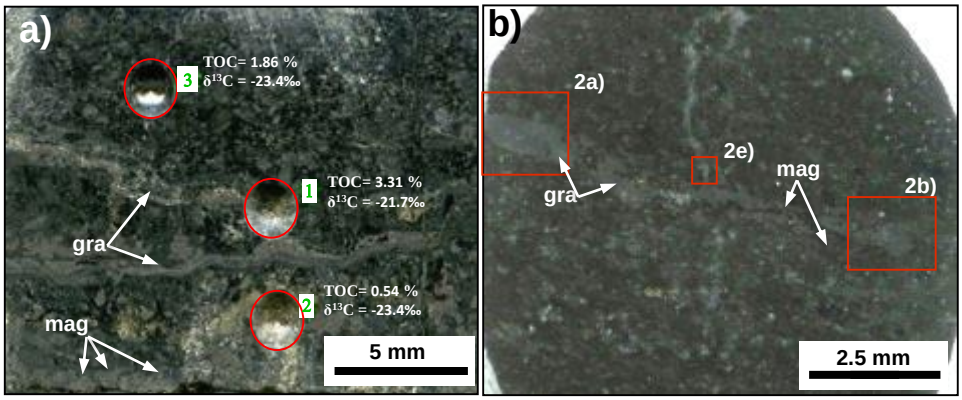

Figure 1: Petrography of graphite in the Michigamme silicate BIF. a) reflected light images of graphite layers in polished slabs where the C-isotope compositions were measured on micro-drilled powders (red circles), b) reflected light image of the round-shape polished slab used for SIMS spot analyses (red boxes 2a and 2b) and FIB-based nanofabrication (box 2e). Mineral abbreviations: gra = graphite, mag = magnetite.

Figure 2 – Papineau et al. (2019)

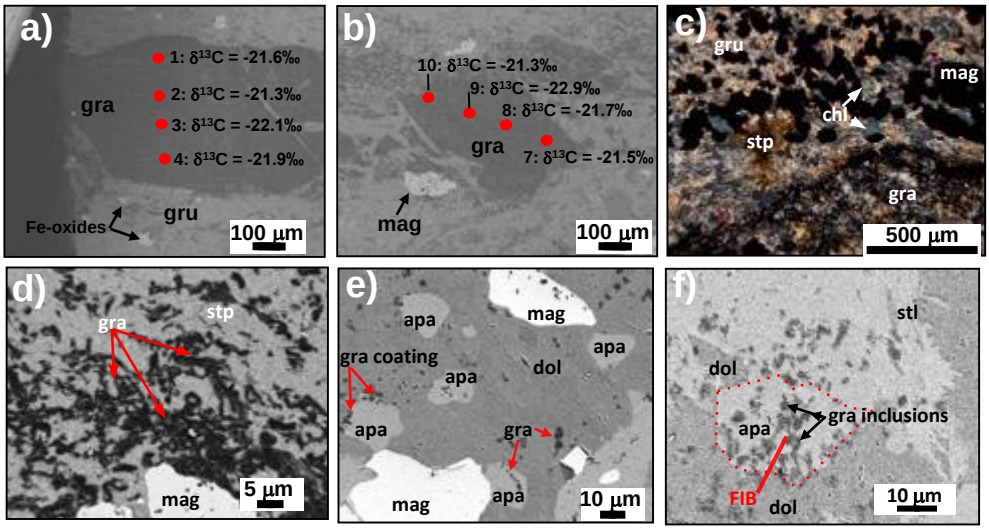

Figure 2: Petrography of apatite and graphite in the Michigamme silicate BIF. a-b) Secondary electron images of spot locations analyzed by SIMS showing the corrected $\delta^{13}C$ values in Table 2, c) cross-polar transmitted light image of the silicate matrix that embeds layers of coarse euhedral magnetite, d) BSE image of graphite filaments in silicate matrix, e) BSE image of apatite grains with graphite coatings in dolomite vein, and f) BSE image of apatite associated with graphite, dolomite, and phyllosilicate, targeted for FIB (lamella location is shown as a red line). Mineral abbreviations: gra = graphite, apa = apatite, cal = calcite, dol = dolomite (Mn and Fe-rich), gru = grunerite, bio = biotite, chl = chlorite, stl = stilpnomelane, mag = magnetite.

Figure 3 – Papineau et al. (2019)

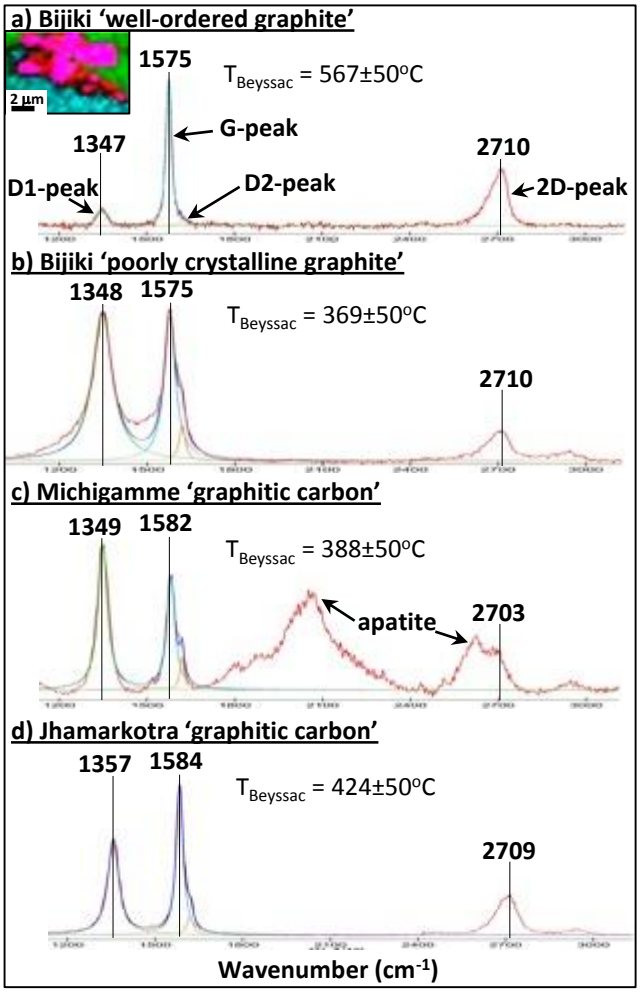

Figure 3: Raman spectra of mixed graphitic carbons in the immediate vicinity the nano-fabricated FIB lamella in Bijiki sample TVA294-659.6 (a-b) compared to other late Paleoproterozoic graphitic carbons (c-d). The inset is a hyperspectral Raman image of Bijiki graphitic carbons showing 'well-ordered graphite' in red (spectrum shown in (a)), mixed with PCG in purple (spectrum shown in (b)), and apatite and carbonate in turquoise and green, respectively. Similar spectra of graphitic carbons from contemporary phosphatic rocks metamorphosed at the greenschist to upper-greenschist facies are shown for comparison in c) for the Michigamme Formation (sample MA0708, Papineau et al., 2017) and d) for the Jhamarkotra Formation (sample UV0807, Papineau et al., 2016). The measured spectra of these graphitic carbons (red) were modelled using a linear combination of Lorentz-fitted peaks (blue) for each of the D1 (green), D2 (orange), and G (turquoise) peaks. Peak metamorphic temperatures were all estimated from the Raman geothermometer of Beyssac et al. (2002), calibrated with minerals in metapelite.

Figure 4 – Papineau et al. (2019)

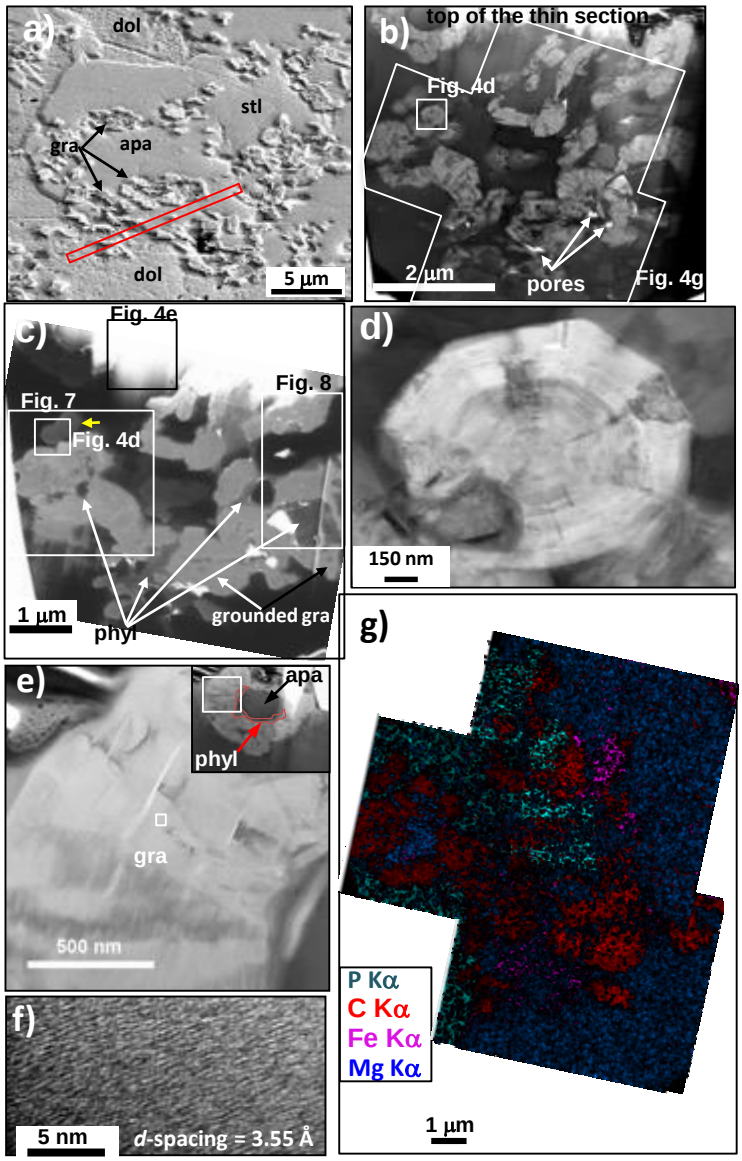

Figure 4: Apatite grain with graphite filaments from TVA294-659.6. a) secondary electron image of the targeted apatite grain, b) bright-field TEM image of graphite (light gray) in the apatite+dolomite matrix (dark gray) prior to Ne thinning – white spots are pores in the rock, c) He secondary electron image which best highlights the thin phyllosilicate (medium gray) coatings on graphite (light gray) inside apatite and dolomite (dark gray), d) cross-section view of concentrically-zoned and well-ordered graphite spherulite, e) longitudinal section of a well-ordered graphite filament associated with phyllosilicate (red area in inset) around and apatite core, f) HRTEM images showing lattice fringes for well-ordered graphite, g) EDS map of four major elements showing the close association of phyllosilicate (purple+blue) with graphite (red) with a legend for colours. Abbreviations: phyl = phyllosilicate, gra = graphite, dol = dolomite, apa = apatite.

Figure 5 – Papineau et al. (2019)

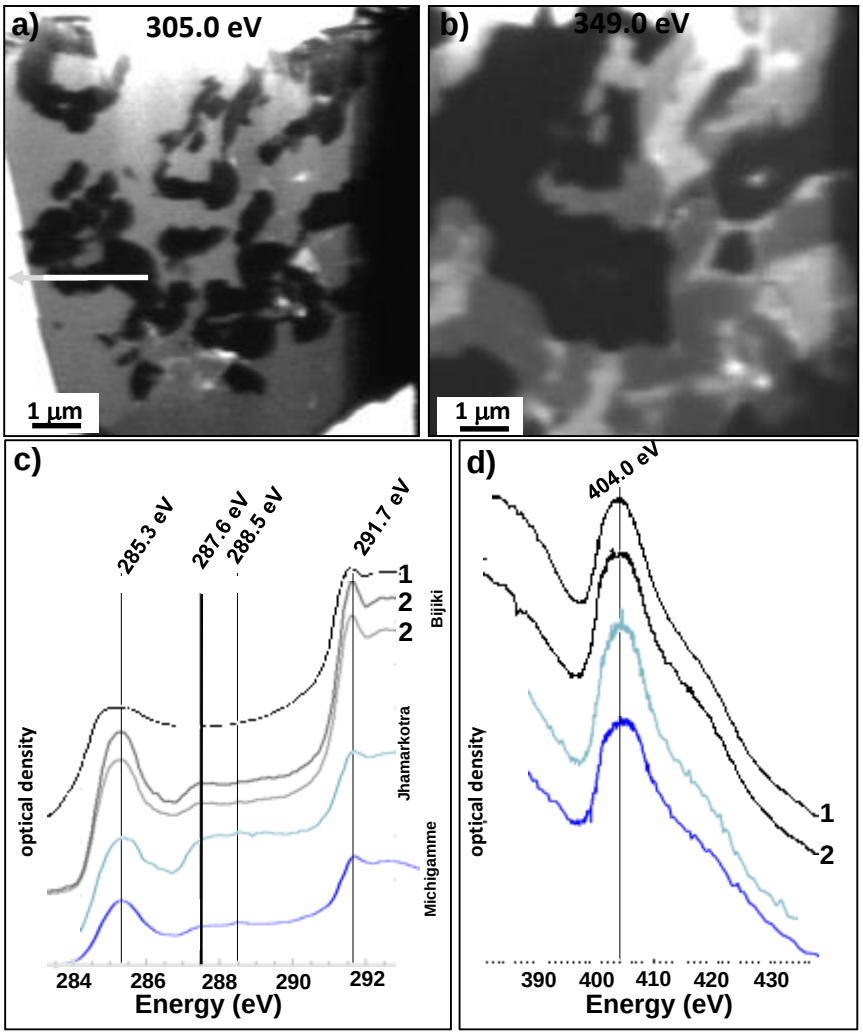

Figure 5: X-ray absorption images and spectra of graphitic carbons with apatite. a) 305.0 eV image, where graphitic carbon is the only phase strongly absorbing photons, hence appearing black. The white part of the arrow represents the line scan over the graphitic carbon (see also Fig. S4). b) 349.0 eV image, where Ca-bearing phases are the strongest absorbers, showing the distribution of Ca in apatite, dolomite (both black) and graphite in the FIB lamella. In this image, phyllosilicate is the brightest phase, closely associated with the distribution of graphitic carbon. XANES spectra at the c) C-edge and d) N-edge with major peaks identified. Graphitic carbons from Bijiki FIB lamella is labelled '1', acid-insoluble Bijiki graphitic carbons is labelled '2', the turquoise and blue spectra are from greenschist facies phosphorite from the Jhamarkotra Formation (turquoise; sample UV0807 from Papineau et al., 2016) and from a phosphatic chert at the Big Eric's crossing locality of the Michigamme Formation (blue; sample MA0708 from Papineau et al., 2017), respectively. Nitrogen was not detected by XANES in the phyllosilicate. See also Fig. S4b-S4e for broader energy context.

Figure 6 – Papineau et al. (2019)

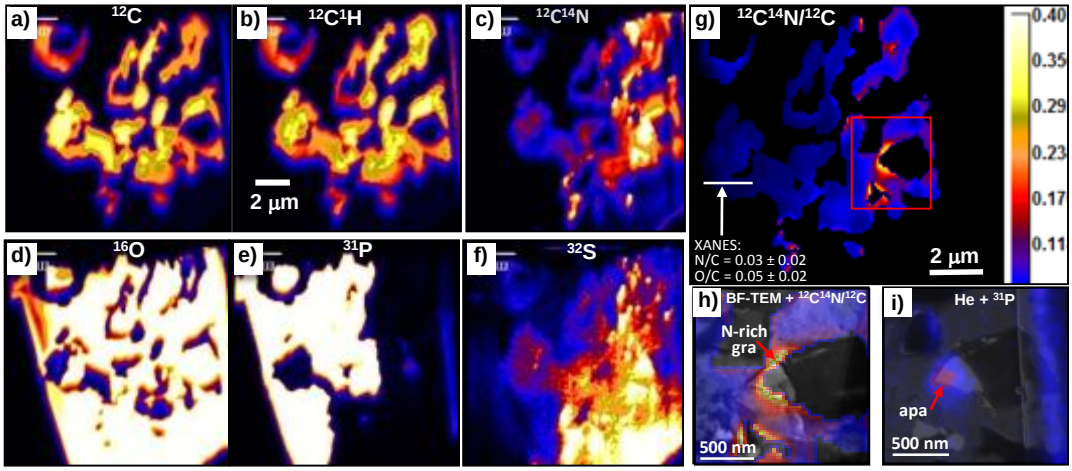

Figure 6: Geochemical context graphite associated with apatite and dolomite in Michigamme Fe-silicate BIF. a-f) NanoSIMS secondary ion images. The distribution of graphite is visible in a) $^{12}C^-$ and b) $^{12}C^1H^-$ images, and the co-location of organic N is shown in c). Dolomite-associated sulphate and the near absence of S in apatite can be seen in f). g) Map of the secondary $^{12}C^{14}N/^{12}C$ ratio calibrated for atomic N/C ratios using XANES data. h) BF-TEM image superimposed by a semi-transparent $^{12}C^{14}N/^{12}C$ map and i) He secondary electron image superimposed by semi-transparent ^{31}P, together showing N-rich graphitic carbon in contact with a nanoscopic grain of apatite. The location of these images is shown by the red box in (g).

Figure 7 – Papineau et al. (2019)

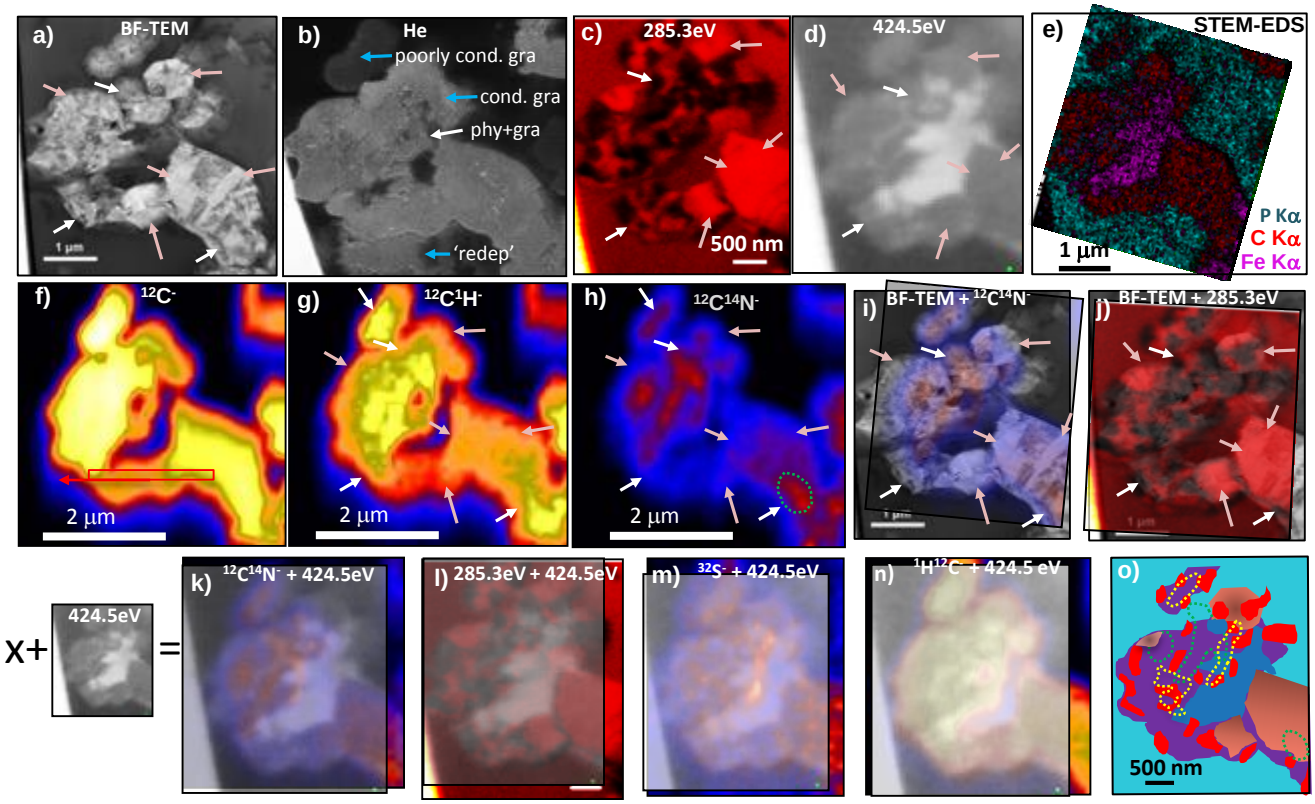

Figure 7: Correlated microscopy of filamentous graphitic carbon from Michigamme BIF that shows disordered graphitic carbon and the well-ordered graphite both correlate to compositionally-specific areas. a) BF-TEM image of the region of interest showing well-ordered graphite (pink arrows) and disordered graphitic carbon (white arrows) as distinguished by sub-domains with variable to random orientations. (b) secondary electron image from focused He beam showing phyllosilicate associated with graphitic carbon as well as highlighting the main contrast differences (blue arrows) in the He image attributed to the good electronic conductivity of re-deposition and parts of the graphitic carbon that are grounded (lightest gray) and poorly conductive graphite surrounded by apatite. X-ray images of graphite showing c) differences in absorption intensity at 285.3 eV are caused by the presence of variably-oriented nanoscopic aromatic domains (black) in disordered graphitic carbon (white arrows), whereas well-ordered graphite (pink arrows) is best highlighted in the brightest red contrast. d) At 424.5eV, the association of well-ordered graphite (pink arrows) and disordered graphitic carbon (white arrows) with less homogeneous gray contrast for the latter. Phyllosilicate is the brightest phase. e) STEM-EDS image of characteristic x-rays showing Fe in phyllosilicate, C in graphite, and P in apatite. Negative secondary ion images of f) ^{12}C, showing homogeneous graphitic carbon (the red box shows the pixels selected for inter-instrumental calibration of atomic N/C, using the corresponding STXM line scan, Alléon et al., 2015), and g) $^{12}C^{1}H^{-}$ and h) $^{12}C^{14}N^{-}$ showing nanoscopic heterogeneities within mostly the disordered graphitic carbon. Images superimposed on a correlated BF-TEM image are i) a secondary ion image of $^{12}C^{14}N^{-}$ and j) an X-ray image at 285.3 eV. Images superimposed over a correlated X-ray image at 424.5 eV, which shows phyllosilicate include: k) secondary ion image for $^{12}C^{14}N^{-}$ showing nanoscopic zones of disordered graphitic carbon and phyllosilicate enriched in N, l) X-ray image at 285.3 eV (in red) showing nanoscopic domains of aromatic carbon excluded from well-ordered graphite in the lower right, m) secondary ion image for $^{32}S^{-}$ showing nanoscopic S-rich disseminations in the disordered graphitic carbon and a more homogeneous distribution in the well-ordered graphite, and n) secondary ion image for $^{12}C^{1}H^{-}$ showing highest H levels in the disordered graphitic carbon. o) Interpretive summary diagram of phases, which shows chemical zones (green dotted line = N-rich and yellow line = S-rich) preferentially located in the disordered graphitic carbon (turquoise = apatite; blue = phyllosilicate; purple = disordered graphitic carbon; pink shaded = concentric or aligned books of graphite; red = highly aromatic carbon).

Figure 8 – Papineau et al. (2019)

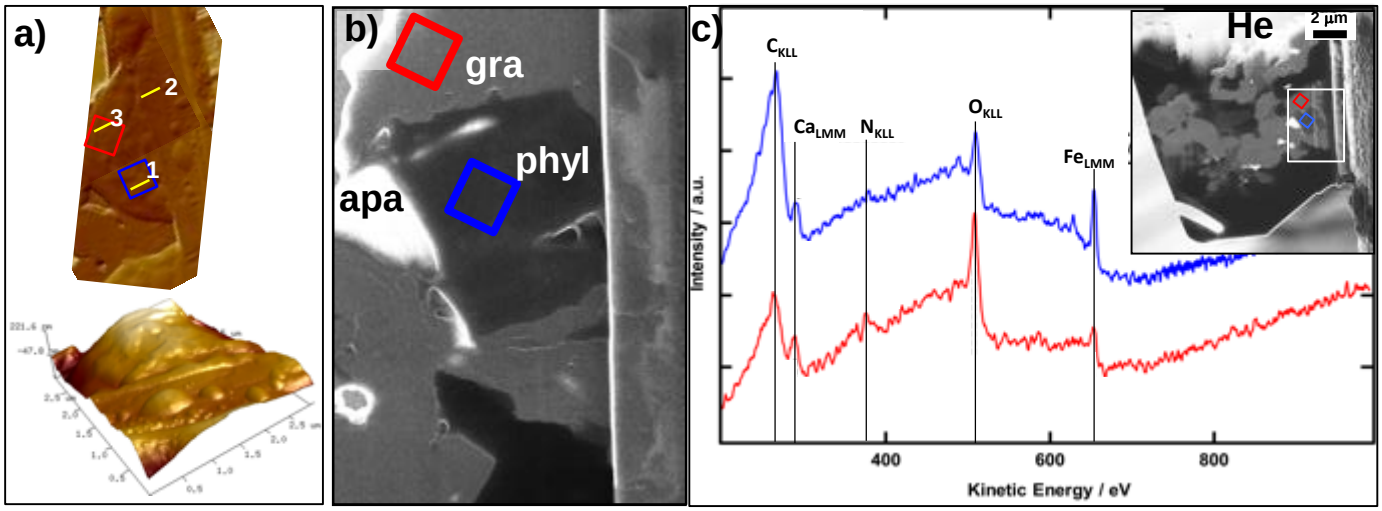

Figure 8: Nanoscale topography of lamella of Michigamme graphite polished using a 400 fA beam of Ne ions and analyzed by AFM and Auger spectroscopy. (a) AFM differential topographic height image of a section of the FIB lamella. Yellow lines indicate the locations of line profiles shown in Fig. S5. (b) He secondary electron image of the area where two spots were analyzed by Auger electron spectroscopy. (c) Two Auger spectra of the blue and red boxes in (b) with the localization in the lamella shown in inset. These show the presence of C, N, O, Ca and Fe in both graphite and the phyllosilicate, although the relative intensity of the peaks is affected by re-deposition on the lamella.